Results in Engineering 29 (2026) 109810

Contents lists available at ScienceDirect

Results in Engineering

journal homepage: www.sciencedirect.com/journal/results-in-engineering

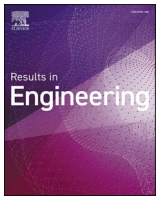

Research paper

Modelling masonry façade cracking induced by non-uniform temperature gradients with soil-structure interaction

Paul A. Korswagen *, Michele Longo, Alfonso Prosperi

Department of Materials, Mechanics, Management and Design, Faculty of Civil Engineering and Geosciences, Delft University of Technology, Stevinweg 1, 2628CN, Delft, The Netherlands

ARTICLE INFO

Keywords:
Clay masonry
Light damage
Cracks
Vulnerability
Temperature-effects
Insolation

ABSTRACT

Temperature effects are frequently cited as the cause of light cracking in masonry façades, yet most modelling studies idealise thermal loading as uniform steps and represent restraint as fully fixed, assumptions that tend to exaggerate damage. This work evaluates whether realistic, non-uniform temperature gradients, like those produced by shading and insolation, together with soil–structure interaction as the dominant restraint mechanism, can generate cracking patterns consistent with field observations. A coupled thermo-mechanical FEM model with a homogenised masonry continuum and tensile softening is employed; the façade–foundation–soil system is modelled explicitly, and damage is quantified using a crack-based index Ψ. A parametric campaign (1200 simulations) spans two façade typologies (clay masonry on unreinforced masonry foundations; calcium-silicate on reinforced concrete strips), three layered soils, 33 geometries, and multiple vertical and two-dimensional gradient shapes. The results indicate that gradient shape is decisive: widely distributed vertical gradients trigger visible damage ($\Psi \geq 1$) at roughly half the temperature differential required by more localised gradients, with visible damage becoming likely around $\Delta T \approx 20$ °C (warming) and ≈25 °C (cooling) for the most adverse shapes. Restraint stiffness governs severity: stiffer sandy profiles increase tensile stresses and cracking, whereas softer profiles accommodate thermal movement; relative to uniform, fully restrained models, crack initiation is delayed by ~15–20 °C and cracking is less distributed. Geometric discontinuities also dominate sensitivity: larger/more openings and low vertical-masonry ratios promote earlier localisation, while overall length/height is secondary. Fragility-like curves provide thresholds useful for assessment and mitigation.

1. Introduction

When most materials experience a change in temperature, they expand or contract [1–3,35]. If this deformation is hindered, internal stresses develop [4,5]; when stress-relieving measures such as expansion joints [6,7,14] are absent, temperature changes may lead to damage [8–10]. Small cracks at building corners, ceiling–wall connections, or around openings are frequently attributed to temperature variations [11–13,51], though these may also reflect settlements, curing shrinkage, or household vibrations [37,48,52]. Correctly identifying the cause is important for assessing the likelihood of further damage, proposing effective repairs, and, where relevant, determining which damages should be indemnified.

1.1. Damage potential due to temperature variations

Older buildings, constructed without stress-relieving measures, are particularly vulnerable. Masonry façades, exposed to sun and weather, experience relatively large temperature variations compared to sheltered elements like floors or foundations [15,16]. In Fig. 1, a historical masonry façade in the Netherlands is replicated with a numerical model where the foundation expands horizontally, leading to strains and stresses in the masonry.

1.2. Overview of mechanical and thermo-coupled modelling of temperature

Modelling the influence of temperature on masonry is a recurring topic [54], yet most studies focus on thermal stress development, deformations, or hygrothermal performance [19,20] without explicitly

* Corresponding author.
E-mail address: p.a.korswagen@tudelft.nl (P.A. Korswagen).

https://doi.org/10.1016/j.rineng.2026.109810
Received 24 January 2026; Received in revised form 17 February 2026; Accepted 26 February 2026
Available online 28 February 2026

simulating crack formation [17,18], though this is often done for concrete [40,43]. Barbero-Barrera et al. [21] examined façade surface temperature modification due to shading, Ferreira et al. [22] modelled coupled thermo-hygro-mechanical behaviour, Resende et al. [9] simulated environmental temperature cycles, and Girardi et al. [1] addressed temperature-induced stresses in heritage arches; none of these capture the crack initiation and propagation that govern visible damage.

The subset of literature addressing cracking under thermal loading is comparatively small. Dilrukshi & Dias [11] showed that restraint stiffness and distribution strongly influence crack location and severity. Bejarano-Urrego et al. [25] found that gradual temperature fields produce more localised damage than abrupt uniform heating. Prakash et al. [26] demonstrated that early-age shrinkage can amplify thermal cracking with stiff supports. Dilrukshi & Dias [8] provided experimental evidence that soil–foundation stiffness plays a critical role: dense sands increased crack severity while soft clays allowed thermal accommodation. More generally, Lagier et al. [15] showed that full-restraint assumptions overestimate stresses, Briffaut et al. [29] quantified the effect of restraint stiffness on crack formation in concrete, and Van Zijl et al. [30] contributed constitutive modelling capabilities (tensile softening, fracture energy, anisotropic damage) in DIANA for coupled thermal–mechanical masonry analysis. These works collectively demonstrate that realistic restraints (including soil–structure interaction), non-uniform temperature profiles, and appropriate material models are necessary for accurate prediction of temperature-induced cracking.

Nevertheless, existing methods share two conservative assumptions: a uniform temperature distribution is applied and restraints are assumed infinitely stiff. A more gradual temperature change and more flexible supports will both produce lower stresses. The stiffness of floors can be reasonably approximated, but foundations are trickier.

The spatial distribution of temperature over façade surfaces is a decisive factor in thermally induced stress development, yet structural models often simplify it to uniform or idealised linear gradients. Empirical thermographic surveys [36,38,23,45,46,56,58] provide detailed evidence of façade temperature variability: González-Aguilera et al. [31] developed photogrammetry-assisted thermography for high-resolution façade temperature mapping; Tejedor et al. [32] refined quantitative thermography for repeatable monitoring; Lerma et al. [33] revealed stable daily and seasonal gradient patterns tied to orientation and shading; and Tavukçuoğlu et al. [34] demonstrated that thermal patterns correlate with damage-prone zones. From a modelling standpoint, Barbero-Barrera et al. [21] showed localised hot spots from shading devices, Resende et al. [13] highlighted persistent vertical and horizontal differentials under diurnal cycles, Ferreira et al. [22] predicted gradient development under different climatic conditions, and Bison et al. [38] captured complex heat gain/loss patterns. Van Zijl et al. [16] demonstrated that non-uniform, empirically derived temperature loads yield markedly different stress distributions compared to uniform fields, while Sazonova et al. [40] and Ferreira et al. [22] offered insights into which gradients are most structurally significant. These works underscore that accurate reproduction of in-situ temperature shapes is a prerequisite for realistic damage modelling.

1.3. Importance of accurate modelling of temperature gradients

A reliable approach to evaluate the damaging effects of temperature gradients on masonry façades serves several purposes: determining whether gradients alone can generate visible damage, establishing which historical designs are most sensitive, guiding the (re)location of dilation joints during retrofitting, assessing repair measures such as self-healing mortars [42], supporting forensic damage assessments, and determining the probable initial condition of a structure before subsequent damaging actions such as settlements or vibrations.

In this paper, we examine the effects of temperature on façades restrained only by the soil underneath the foundations, without the conservative assumptions of uniform loading or infinite restraint. Temperature gradients over façades arise from solar radiation, shading, wall orientation, and heat flux towards roof or foundations; gradients with small absolute differentials are not uncommon. Fig. 2 provides an example where shading and cooling at the bottom of a wall generate a 20 °C differential across the load-bearing wall. While a large contrast is also observed against the perpendicular façade, this paper focuses on gradients within single façades as this topic has yet to be sufficiently explored.

1.4. Novelties and overview of paper

The novelties of this work are: 1) we explore the effects of temperature gradients within masonry façades; 2) we employ realistic, non-conservative restraints; 3) we quantify crack-based damage via the parameter Ψ; 4) we vary gradient profiles, material properties, and façade geometries to parametrically explore their influence; and 5) based on these variations we estimate the probability of visible damage due to temperature differentials.

This paper starts with an overview of the modelling method focused on predicting cracks in masonry façades when exposed to temperature changes. To explore parameter sensitivities, multiple façade geometries, supporting soils, and temperature gradients are included. Results are presented in Section 3, where damage patterns from positive and negative temperature changes are also contrasted. In Section 4, results are interpreted and discussed while limitations are examined. Finally, conclusions are highlighted in the last section.

2. Modelling approach

In this section, we first establish cracking because of temperature-

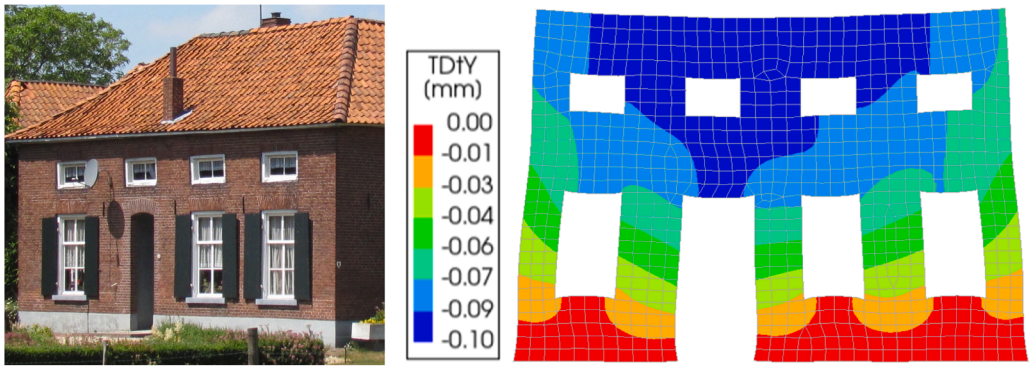

Fig. 1. Example of a recognised historical masonry façade in the Netherlands, left. Right, a 2D model of the front façade subjected to a horizontal strain at the base and showing its exaggerated deformed shape with a contour colouring of vertical displacements. This façade inspires a few of the façade geometries studied in this work.

Fig. 2. Temperature on a façade from a thermographic image. The photograph shows a different temperature between neighbouring walls and a stark temperature decrease where the façade is in the shadow. Own images, see also [69].

induced stress. Then, we explore cracking in masonry and how it can be modelled within a Finite-Element-Method (FEM) strategy and establish the material model for the masonry façades. Next, we look at the support and restrain provided by the soil [41,44,39] and assemble the façade model upon which to evaluate the effect of the temperature gradients. Note that we focus on temperature gradients or differentials which could be explored in °Celsius or Kelvin interchangeably.

2.1. Thermo-mechanical basis and damage measure

The relationship between temperature and induced stress on the masonry can be captured by combining two known physical equations in the case where the extension of the object is fully restrained:

$$\varepsilon = \frac{\Delta L}{L} = \alpha \cdot \Delta T \tag{1}$$

$$\sigma = E \cdot \varepsilon = E \cdot \alpha \cdot \Delta T \tag{2}$$

where α is the thermal expansion constant, ΔT is the change in temperature, L is the length of the object, E is the Young's Modulus of the material, and ε and σ are the strain and stress, respectively. If a masonry wall serving as a fence were built and anchored to a building on each end, a ΔT of 15 °C would result in a stress higher than the horizontal tensile strength of most fired-clay brick masonry ($f_{t\ h} = 0.3$ MPa, $E = 4$ GPa [57]) which would cause the masonry to crack (with $\alpha = 7.6^{-6}_{10}$). At that stage, the horizontal stresses would be unloaded, and the deformation would concentrate in a vertical crack of 1 mm in width (for a fence of $L = 10$ m). These equations are for the one-dimensional problem but may be expanded to the two-dimensional situation for the finite-element approach; see next.

The cracking behaviour of masonry façades is more complex, though cracks are a common expression of damage in masonry; see Fig. 3. The wider the crack, the more severe the damage may be categorised. Cracks on façades do not always correspond to structural damage but will still compromise the watertightness of the structure and its aesthetics, potentially affecting the perception of safety of its users [61]. When several cracks are present, determining the damage severity is more cumbersome; in this study, the damage parameter Ψ is used. The parameter summarises crack-based damage in masonry by considering the number of cracks (n), and the cracks' width (c_i) and length (L_i) as per

Fig. 3. Photographs of cracks in bare masonry walls. (a)Small crack narrower than 0.5 mm; (b)crack approximately 2 mm wide; (c)crack narrower than 2 mm; and (d)wider than 5 mm. Adapted from SBR [60].

Eq. (3):

$$\Psi = 2 \cdot n^{0.15} \cdot c_w^{0.3} \text{with} c_w = \frac{\sum_{i=1}^{n} c_i^2 \cdot L_i}{\sum_{i=1}^{n} c_i \cdot L_i} \quad (3)$$

A value of Ψ=1 corresponds to the lower threshold of visible damage with cracks of up to 0.1 mm in width; damage at Ψ<1 is not perceivable. Ψ=2 is linked to cracks about 1 mm in width, which are easily detected but also easily repaired. Ψ=3 can be linked to the end of light damage, with cracks around 5 mm wide; larger values of Ψ will require invasive interventions for repair and may also necessitate structural repairs.

Cracking in masonry has been investigated in several studies [48–50]. Several experiments, focusing on the initiation and propagation of cracks on masonry walls, have contributed to calibrating numerical, computational models. Fig. 4 shows a full-scale masonry wall surveyed with Digital Image Correlation and subjected to an in-plane horizontal drift leading to small, automatically-detected cracks.

2.2. FE model of masonry and thermo-mechanical coupling

Cracks in masonry can be replicated, and later predicted, using (3D) FEM models. In this study, the response of masonry façades to temperature effects is modelled. The façade-scale cracking behaviour is simulated using a continuum material approach. In this approach, the masonry composite is homogenised over regular finite elements as depicted in Fig. 1. In this way, the method captures the masonry's response under both compression and tension through a defined stress-strain relationship, as illustrated in Fig. 5. In tension, once the tensile strength is exceeded, the material undergoes rapid softening until it reaches zero residual strength, effectively representing a fully developed crack. Specifically, quadratic solid elements (CHX60) are employed, utilising the Total Strain Rotating Crack Model (TSRCM, [53,62,59]) to represent the homogenised, smeared constitutive behaviour of masonry. The adopted material properties are characteristic of older, fired-clay brick (CL) façades commonly found in the Netherlands [57]. The masonry is assigned a density of 1900 kg/m^3, a Young's modulus of 5 GPa for CL and 4 GPa for CS, and a Poisson's ratio of 0.25 for its elastic range. For tensile behaviour, a strength of 0.1 MPa is used along with a fracture energy of 8.1 N/m using an exponential softening curve, combined with the Govindjee [47] crack-band-width criterion. Similarly, the compressive strength is set at 8.5 MPa and 7 MPa, for CL and CS respectively, with an associated fracture energy of 18.4 kN/m based on parabolic softening; see Fig. 5. The façade elements are meshed at 200 × 200 mm. The thermal expansion parameters are 7.6μ for CL, 8.1μ for CS, and 10μ for concrete.

The Total Strain model includes temperature coupling by decomposing the total strain into the temperature and mechanical components, see Eq. (4). The temperature component is simply the temperature change multiplied by the coefficient of thermal expansion as per Eq. (1). In this way, the constitutive model stops being strictly a "total strain" model, though temperature effects can thus be easily included [71].

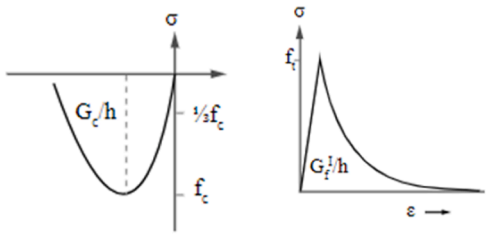

Fig. 5. Stress-strain relationships for compressive and tensile behaviour, respectively, for the constitutive material model employed: the Total-Strain Rotating Crack Model [71].

$$\epsilon_{tot} = \epsilon_{\Delta T} + \epsilon_{mec} \quad (4)$$

2.3. Restraint modelling and soil–structure interaction

Having established the material model for the masonry of the façades, their support and restrain must be defined, too. First, over-restraining the façades is undesired since temperature-induced stresses only arise in reacting to hindered deformations. For this reason, the restraints provided by floors or roof elements are not considered. Besides, for older structures, these are constructed out of timber which provides limited stiffness and thus restrain. Similarly, foundations are explicitly included in the models instead of being represented with line elements or boundary interfaces. In this manner, they are also affected by the temperature surface gradient and are deformed, stressed, and cracked accordingly.

The restrain to the temperature-induced expansion/contraction is provided by two aspects in the models. First, due to the gradients themselves, portions of the façades would be subjected to a different temperature and thus would expand or contract to different degrees. I.e. for an increase of temperature, the portions subjected to the larger increase would be restricted by the cooler portions which would themselves be forced to expand by the warming parts; cracks would likely appear in these cooler areas subjected to tension.

Second, buildings are, of course, supported by foundations resting and embedded in the soil. The soil itself, unaffected by the temperature gradient, will provide some restraint to the façades. In fact, the stiffer the soil, the more restraint it will enforce. This is illustrated in Fig. 6, where three situations are compared. When the building is stiffer than the soil, as it usually the case for undamaged buildings, the soil surrounding the buildings adapts to its movements; however, if the soil is relatively stiff or the building is flexible, perhaps due to existing cracks, the building and soil will deform similarly. Hence, stiff sandy soils, historically well suited for strip (masonry) foundations found in older façades, would work against the temperature-induced deformations, while softer soils would allow such deformations without inducing stresses.

Consequently, the modelling strategy employed herein includes variations of the layered soil to quantitatively verify their distinct

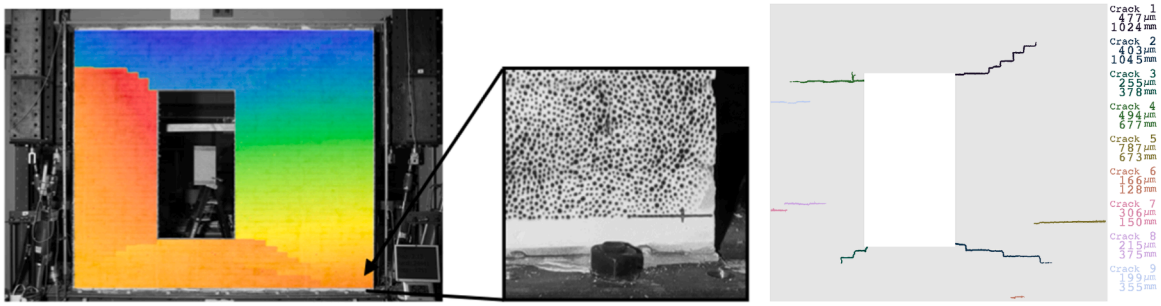

Fig. 4. Cracking from experiment on a full-scale masonry wall surveyed with Digital Image Correlation. Overlaid displacement contour (left), black and white speckle pattern (centre), and automatic crack detection with Ψ=2.3 (right). Note that left and right images do not belong to the same specimen.

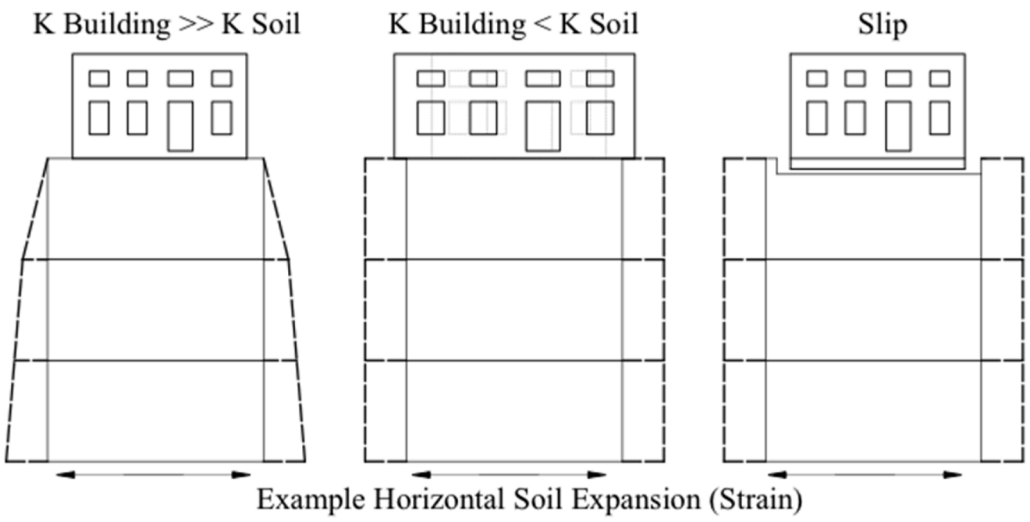

Fig. 6. Soil-building interaction in the context of stiffness differences. K stands for the stiffness of the building or of the soil. In this example, a horizontal deformed is enforced at the bottom of the soil column.

restraining effect on the façades. The model is thus built up as presented in Fig. 7 (and later Fig. 10). The masonry façade, with unreinforced masonry foundations and interlocked transversal masonry walls, is placed atop a layered soil block, of which three variations are analysed: a fully sandy profile (labelled Soil #6 in reference to a study with representative Dutch soil profiles [64]), a clay-peat-sandy profile (Soil #9) and a clayey-sandy profile (Soil #0) with a stiffness value (at the foundation) in between that of the other two profiles. The illustrated façade corresponds to that of the historic building introduced in Fig. 1. Its foundation is embedded in the soil block, and a no-tension Coulomb-friction interface is placed between these: it allows separation under normal tension but transfers shear forces through friction, with stiffness and strength parameters adopted from the calibrated settlement models of the same façade typologies reported in [65]. As noted in [65], such an interface restricts crack propagation perpendicular to the contact and limits sliding at the foundation base through its shear stiffness and strength. In the present study, however, the restraint is governed primarily by the explicitly modelled non-linear soil block rather than by

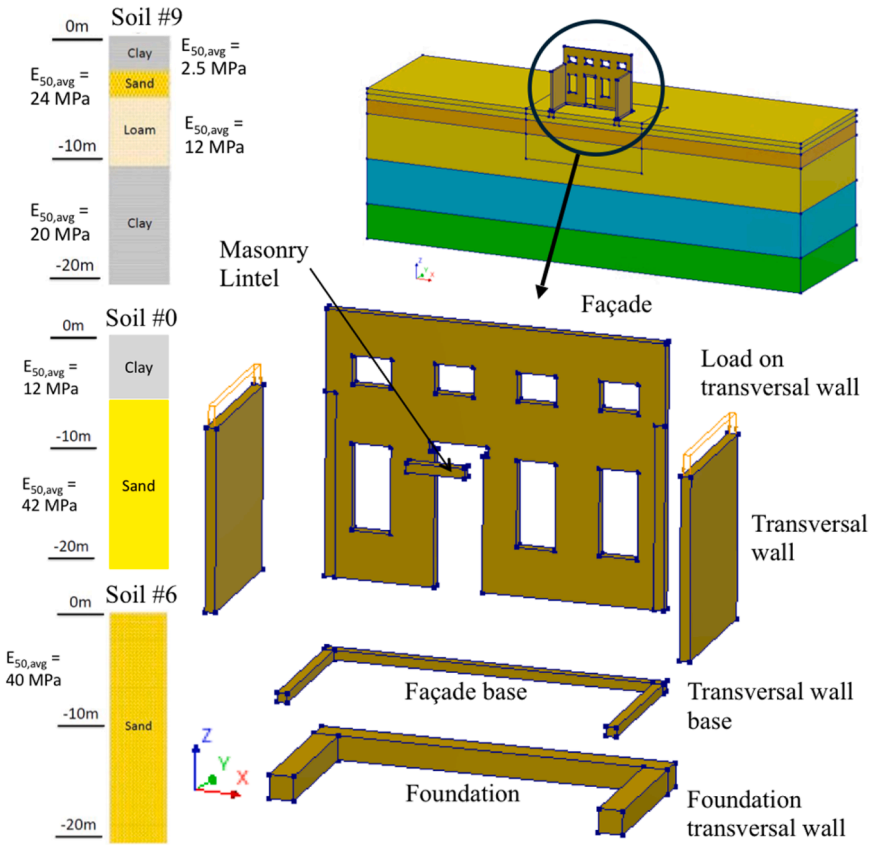

Fig. 7. Left, three soil profiles, Soil #9, #0, and #6, with approximate Young's moduli (E50: reference triaxial secant stiffness). Centre, exploded façade model for fired-clay masonry with idealised, unreinforced masonry foundation embedded in the soil block.

the interface alone which only plays a minor role with its no-tension option; the sensitivity of the interface properties has was varied and found to be unimportant due to the presence of the non-linear soil. The model is symmetric at the centre of the building on a plane parallel to the façade. The dimensions of the soil block (45 × 15 × 12.5 m, LxHxW) were chosen such that the presence of the building did not affect the outer soil elements of the block.

Furthermore, the soil in the models is considered non-linearly via the "small strains hardening soil" constitutive model. This model presents a higher stiffness for small strains [72] which is particularly important with temperature deformations, for which strains are typically low, and when the soil-structure interaction may actively hinder the temperature-induced deformations, thus causing stresses on the façades. Indeed, in this situation, is better to err with slightly higher Young's moduli, as the stiffer soil will provide a higher restraint. The small-strains soil model requires multiple parameters, which are varied in depth and are presented in Tables 1–3 for the various soil profiles. The tables show that the initial stiffness of the soil is higher (E0), providing constraint against the temperature-induced strains. The upper soil layers are meshed starting at 400 to 750 mm while the lower layers are 1250 mm, all with quadratic elements.

2.4. Thermal loading: gradient families and application

The temperature gradients applied to the buildings comprised essentially two variations: a gradient purely in the vertical direction, for which the temperature of the façade changed with its vertical coordinate Z; and, a two-dimensional gradient, changing both in the plane of the façade (X) and in Z. The gradients studied considered both positive (increasing temperature) and negative (decreasing temperature) profiles. Three gradient shapes were assigned to the profiles: a linear shape (Shape 2), a parabolic shape with the highest gradients at the bottom of the façade (Shape 1), and a parabolic shape with the largest gradients at the top of the façade (Shape 3). The temperature gradients are shown in Fig. 8 including the parabolic function. Note that the gradient shape function includes the foundation of the building and that the normalised temperature shapes range from 0.05 to 1.00 over the façade which translates to a maximum differential of 1.00 in respect to the soil block. The temperature differential is amplified by up to 40 times, corresponding thus to a maximum differential of up to 40 °C. The upper bound of 40 °C for the applied temperature differential does not represent an expected or target scenario; rather, it defines the range of the incremental analysis. Each model is loaded in small steps from 0 to 40 °C, and damage is recorded at every increment, analogous to a force–displacement pushover analysis in which the imposed displacement far exceeds the expected failure point. The analysis is deliberately extended to a high differential so that the full evolution of damage (from crack initiation through visible cracking) can be captured without prescribing a priori the critical threshold. As the results later show (Figs. 13 and 17), visible damage ($\Psi \geq 1$) typically develops between 15 and 25 °C, well within the analysed range; the 40 °C ceiling simply ensures that no relevant behaviour is truncated. The thermal load is analysed after a gravity and overburdened phase have been resolved. The temperature is constant through the thickness of the wall and follows strictly the tensor value of the applied field.

2.5. Reference models and parametric campaign

To evaluate the models, two additional models without the soil block were analysed. These are presented in Fig. 9 and comprise a model where a uniform temperature differential is applied to only the foundation or only the façade. These models, more akin to those more commonly found in literature [1,2,8,30], serve to validate and compare the modelling strategy adopted. Moreover, they help to quantify the effect of including soil-structure interaction and applying gradual temperature gradients when analysing temperature effects on façades.

Several variations were included in the modelling campaign. Besides the soil profiles and temperature shapes described, the building material was varied. In addition to the fired-clay façade with unreinforced masonry foundation, a set of calcium-silicate brick masonry façades on reinforced concrete strip foundations was studied (see Fig. 10). These constitute the two façade general typologies studied. Further, façade geometries were varied to include more or fewer openings, larger openings, varying length/height ratios and gable shapes. In total, 33 geometries are shown in Fig. 11, and their properties are gathered in the supplementary material. Besides the opening ratio, a vertical masonry ratio is included. This represents the minimum ratio of masonry present on any vertical line in the façade.

With these variations, a large number of permutations were generated: comprising the 3 soil profiles, 4 temperature shapes, 2 warming or cooling temperatures, 33 façade geometries, and 3 material sets corresponding to a weak, standard, and strong set of material properties for each façade, where strength and stiffness are reduced/increased by 50 % in respect to the standard set. These 1200 model results, with each model incrementally loaded from 0 to 40 °C in small steps, give a wide picture of the relationship between temperature effects and crack-based damage to masonry façades. The results are analysed in terms of specific damage patterns and pooled together to observe trends or the effects of particular parameters. Moreover, the large number of results allow observations about the probability of damage.

3. Results

It is not feasible to present in this publication the deformation and damage patterns of all 33 façades investigated. Instead, in Fig. 12, a menagerie of cracking examples is collected for different façades subjected to distinct gradient shapes. On the first row, a cooling profile is applied: the top right corner of façade 1A cools the most; accordingly, it also contracts the most. This corresponds to gradient Shape 1 in 2D (see Fig. 8). While several finite-elements at the corners of the windows exceed their tensile strength, a visible crack appears only on top of the door opening, on the left side of the façade - not where the highest temperature difference was applied. Similarly, the second row presents the opposite situation, where the top right corner warms up the most. In this case, the main crack appears at the top centre of the façade. This is because the expansion of the masonry at top of the façade, restricted by the bottom of the façade, causes bending where tensile stresses appear at the top.

The next three rows in Fig. 12 consider façade 2B, a long façade with large openings. All three cases are of cooling though with different 2D gradient shapes: with most of the gradient occurring towards the bottom

Table 1
Derived values for input corresponding to the clay soil profile (#9) for the small-strains hardening soil model. Values in MPa where required. For variable names, see [72].

#	Depth [m]		Type	E50	Eoed	Eur	E0	pref	POP	c	φ[°]	ψ[°]	K0	γ0.7
1	0.0	-3.0	Clay	2	2	10	72	0.1	0.01	0.005	23	0	0.62	1E-04
2	-3.0	-5.3	Sand	24	24	96	216			0	35	5	0.43	
3	-5.3	-11.3	Loam	12	12	48	108			0	30	0	0.50	
4	-11.3	-28.5	Clay	19	19	77	288			0.001	28	0	0.54	
5	-28.5	-30.7	Sand	180	180	720	1620			0	40	10	0.36	

Table 2
Derived values for input corresponding to the sand soil profile (#6) for the small-strains hardening soil model.

#	Depth [m]		Type	E50	Eoed	Eur	E0	pref	POP	c	φ[°]	ψ[°]	K0	γ0.7
1	0.0	-1.1	Sand	36	36	144	324	0.1	0.01	0	40	10	0.36	1E-04
2	-1.1	-2.5		24	24	96	216				35	5	0.43	
3	-2.5	-7.0		36	36	144	324				40	10	0.36	
4	-7.0	-11.5		90	90	360	810				40	10	0.36	
5	-11.5	-16.8		18	18	72	162				35	5	0.43	
6	-16.8	-21.9		210	210	840	1890				40	10	0.36	

Table 3
Derived values for input corresponding to the sand soil profile (#0) for the small-strains hardening soil model.

#	Depth [m]		Type	E50	Eoed	Eur	E0	pref	POP	c	φ[°]	ψ[°]	K0	γ0.7
1	0.0	-6.0	Clay	12	12	48	180	0.1	0.01	0	25	0	0.58	1E-04
2	-6.0	-15.0	Sand	42	42	168	378				40	10	0.36	

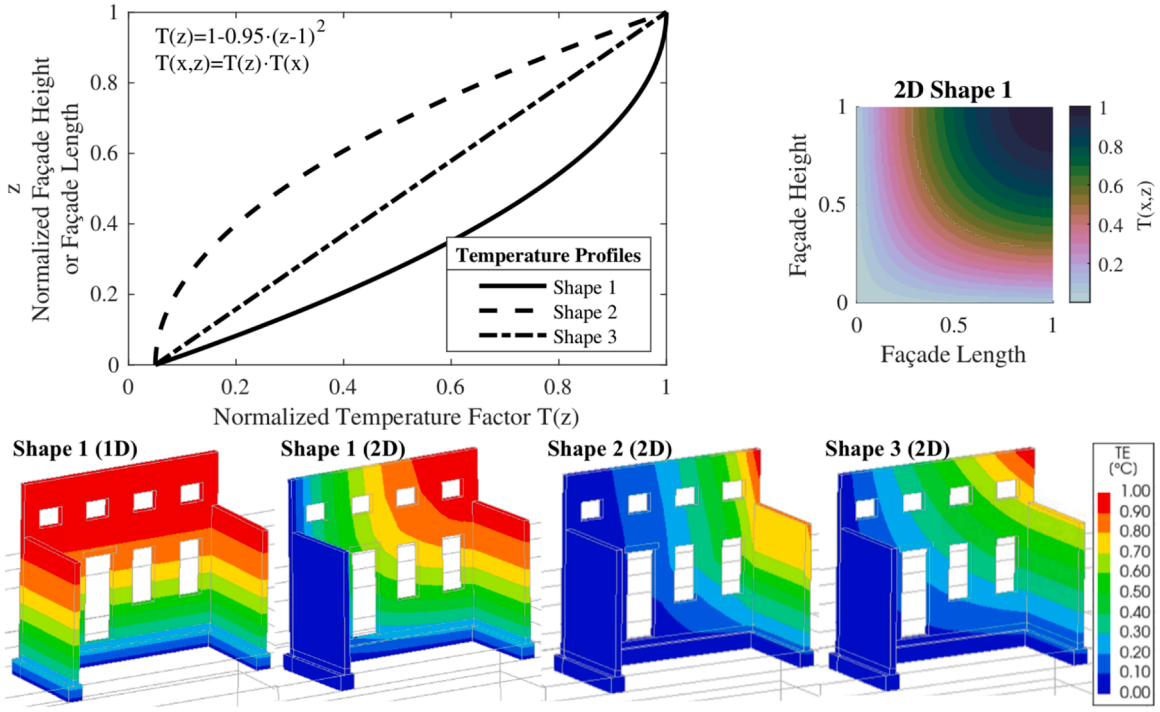

Fig. 8. Temperature profiles or gradient shapes on a façade. Three functions are applied vertically or horizontally to produce four distinct gradient shapes.

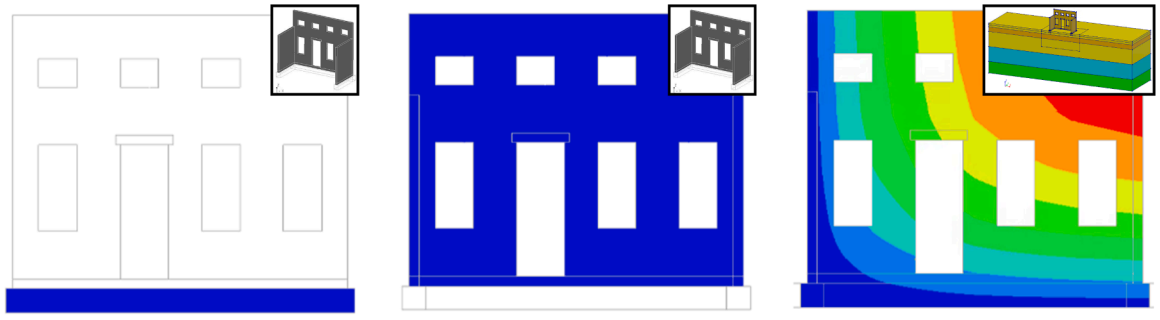

Fig. 9. Model Types. Left, façade model without soil where a temperature differential is applied only at the foundation; middle, ditto but the differential is applied only to the façade. Right, full model with soil, foundation, and façade with gradual temperature differentials (gradient shapes).

(Shape 1), the top (Shape 2), or linearly distributed (Shape 3). The cracking patterns are similar, consisting of aligned vertical cracks at the corners of windows splitting the façade in half. The first shape causes more distributed cracking but is otherwise similar to the other shapes. In terms of damage intensity, all three cases reach a Ψ value of 2.5; while Shape 1 produces slightly narrower cracks, the larger number of cracks

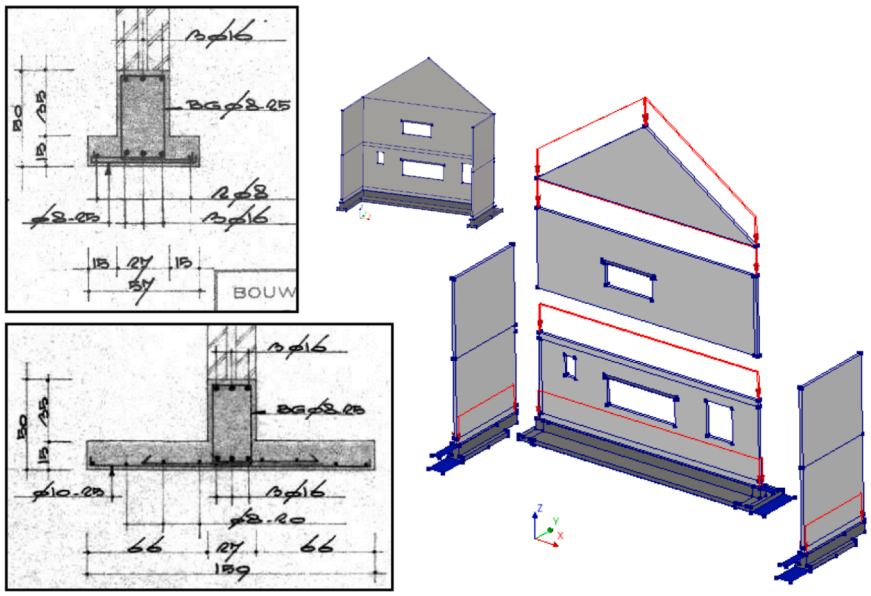

Fig. 10. Exploded CaSi façade with strip-plate reinforced concrete foundations.

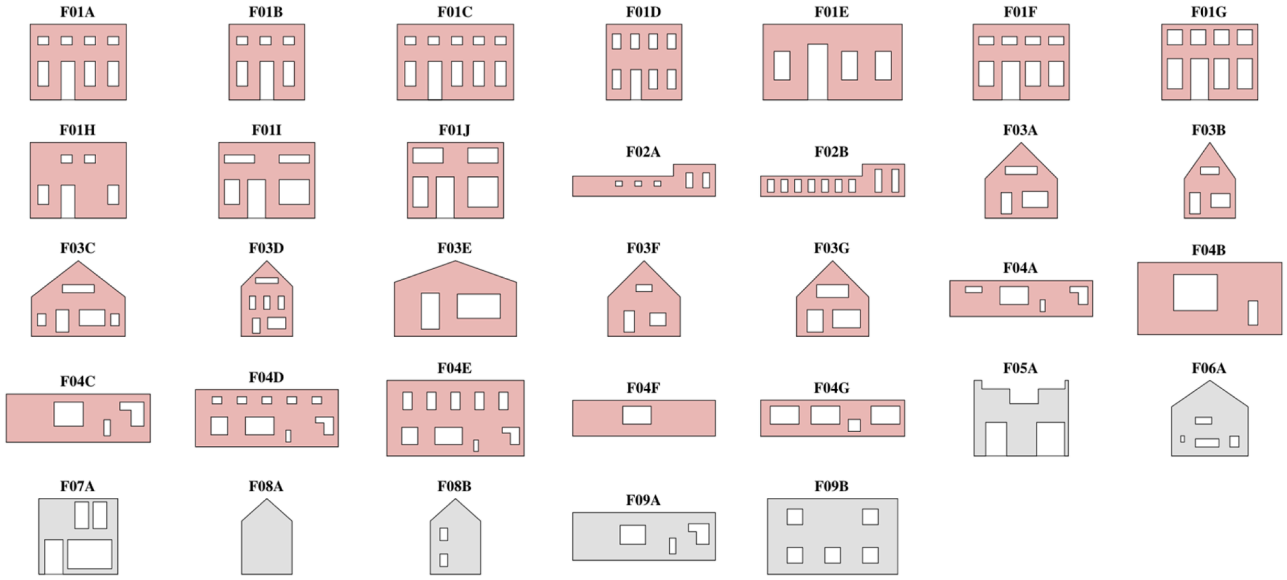

Fig. 11. Façade geometries: in pink, fired-clay brick, and in grey, calcium-silicate brick masonry. The dimensions of the façades are provided in a dxf file, supplemental to this text.

means that damage is evaluated with the same Ψ value, see Eq. (3). The bottom row shows two results for façade 3F. In this case, cooling leads to a crack at the bottom of the façade as the contraction at the top forces the façade to deform.

3.1. Pooled response: mean damage–temperature relationship

The temperature-damage curves from all the models can be collected to determine a mean response of masonry façades to increasing or decreasing temperature gradients. This is illustrated in Fig. 13 and some observations stand out. First, there is a large variability between all the models, but the mean behaviour is fairly linear with damage starting from 5 °C onwards but becoming visible at 20 °C or 25 °C for warming or cooling respectively. Indeed, the curves show that façades are more sensitive to damage for warming gradients than cooling ones though cooling gradients are more likely to generate invisible damage ($\Psi<1$).

3.2. Sensitivity to key parameters

The large variability of the façade sensitivities requires a more careful examination of the various parameters. This is done by obtaining the mean response of segregated categories. First, in Fig. 14, the influence of the gradient shape is explored for a sub selection of the façades. This reveals that Shape 1, in either its purely vertical (1D) or 2D variants, is the most damaging, with similar damage intensities developing at temperatures that are half or a third of those required to cause damage when gradients are more in the form of Shapes 2 and 3. This is not unexpected since both types of Shape 1 cause a larger region of the façade temperature to change. Again, for cracks narrower than 0.1 mm ($\Psi<1$), cooling gradients were more damaging than warming gradients. For the 40 °C differential investigated, the other two shapes, in average, didn't lead to visible damage. For this reason, only the indicated façades were explored with these shapes.

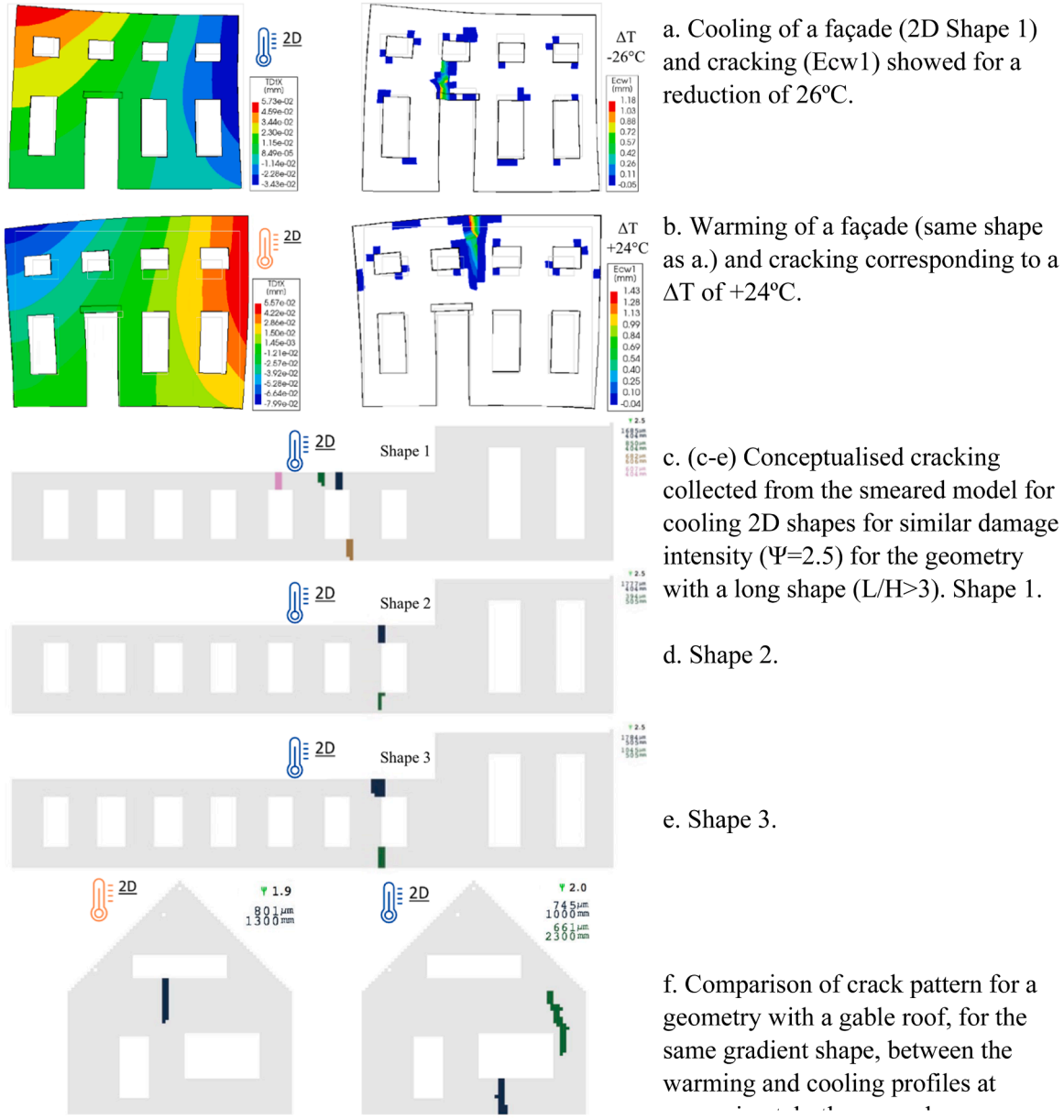

a. Cooling of a façade (2D Shape 1) and cracking (Ecw1) showed for a reduction of 26ºC.

b. Warming of a façade (same shape as a.) and cracking corresponding to a ΔT of +24ºC.

c. (c-e) Conceptualised cracking collected from the smeared model for cooling 2D shapes for similar damage intensity (Ψ=2.5) for the geometry with a long shape (L/H>3). Shape 1.

d. Shape 2.

e. Shape 3.

f. Comparison of crack pattern for a geometry with a gable roof, for the same gradient shape, between the warming and cooling profiles at

Fig. 12. Example damage patterns from a few model cases.

Next is a comparison between the façades with (CSBR) and without (CLBR) reinforced concrete foundations. The latter have unreinforced masonry foundations and seem slightly more vulnerable but not significantly so. There is also not much influence due to the material set, expect for the weak material set on the reinforced foundations. The weaker material has a lower tensile strength but also a lower stiffness, which makes it more flexible. Hence, this group more easily adapts to the deformations imposed by the temperature effects and its tensile strength, mostly needed at the bottom of the façade for cooling gradients, is provided by the steel reinforcement bars in the foundation. For the same group without reinforcement (CLBR) the most vulnerable set is indeed the weak set.

Finally, Fig. 14 compares the three soil profiles further segregated by gradient shape. For visible damage (Ψ≥1), the stiff soil (#6) leads to a stark difference in damage between the positive and negative temperature gradients; it prevents the façade from contracting (negative) and keeps the façade from expanding (positive); in this way, it limits cracking for both scenarios. The soft soil (#9) doesn't modify the behaviour of the façade much and thus lies in between the lines for Soil 6. The average soil (#0) appears closer to the upper bound set by the stiff soil. The purely vertical gradient generates larger differences (of 15 °C for Ψ=1 for the average response) between the various soil profiles; the two-dimensional gradient shapes only vary in half that temperature.

Other interesting comparisons concern the geometrical features of the façades. Fig. 15 segregate the average of the results by the number of openings, opening ratio, vertical masonry ratio, and length/height ratio. Most behave as expected, though their quantifiable influence on the response for Ψ=1 is a key outcome of this figure. The more openings a façade has, the more vulnerable it is to temperature effects. Indeed, the curves for zero openings are 10 °C to 25 °C less vulnerable than those with eight openings. Cooling temperature shapes are more affected by the number of openings than warming profiles. The opposite is true when considering the opening ratio; in this case warming profiles are most affected by a different opening ratio. However, the expected outcome, that a higher ratio of openings, up to 50 % of the façade dedicated to openings illustrated in the figure, will reach visible damage 20 °C earlier than a façade with no openings, and that the other two ratios fall in between, is shown. For the cooling profiles, the opening

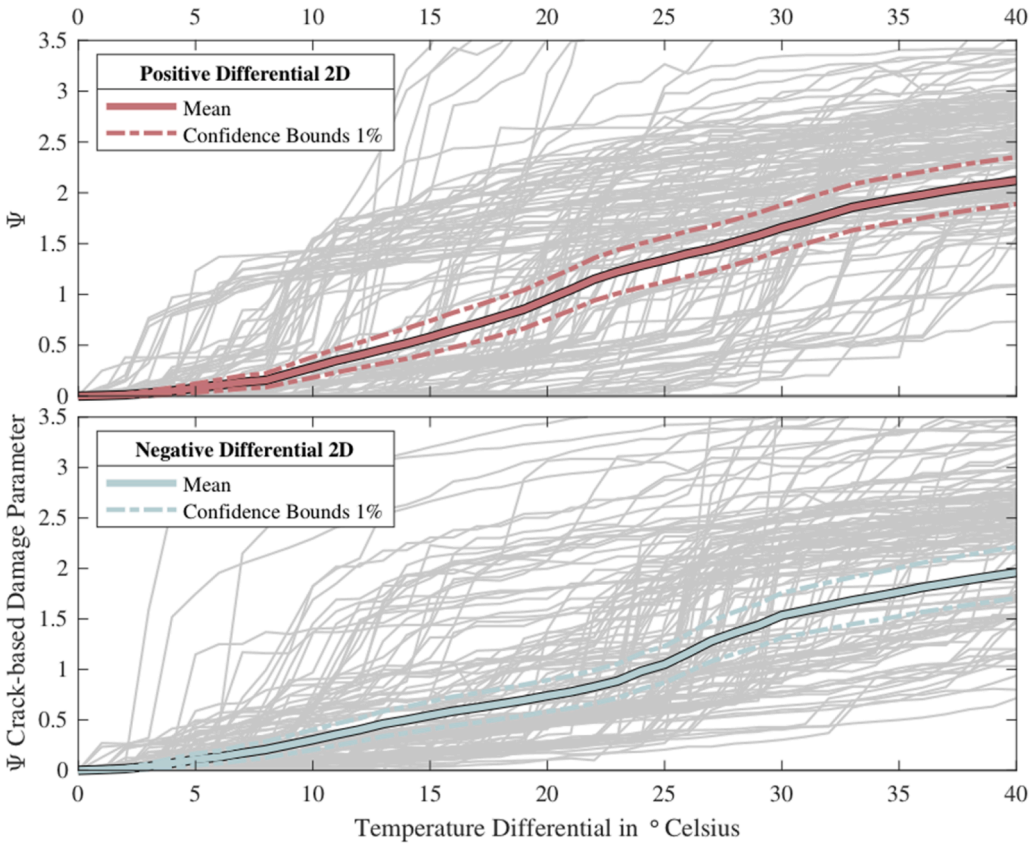

Fig. 13. Mean damage (Ψ) vs. Temperature differential. Confidence of the mean is shown.

ratio seems irrelevant regarding damage sensitivity. While the two graphs (number of openings and opening ratio) are related, the comparisons with the opening ratio are made between façades with similar number of openings to only contrast the parameter of opening ratio.

The vertical masonry ratio shows a similar picture. When the minimum ratio of masonry on any vertical line is high (80 % in the graph), meaning that few openings are aligned on top of each other, the façades are less vulnerable to warming temperature changes. As the amount of masonry goes down, the façade becomes more vulnerable with a 15 °C difference for Ψ=1 between 80 % and 20 % of masonry.

For cooling temperature changes, the behaviour is opposite: more masonry is detrimental. This is somewhat unexpected. However, a careful inspection of the deformation and cracking plots (as shown in Fig. 12) suggests an explanation. When the façades are contracting at the top, less masonry means that there is also less shear stiffness provided by the piers to restrict this deformation. If the deformation is thus free to occur, no stresses nor cracks develop. Note that his inverted trend is also observed for the segregation by opening ratio but less significantly.

Finally, Fig. 15 compares the length over height ratio. Longer façades, with a higher L/H ratio, seem more vulnerable for cooling and less for warming gradients. However, from the four geometrical features presented, the L/H is the least influential one. This stands in contrast to damage from settlement actions for which the L/H is the most influential parameter [65].

3.3. Benchmarks and fragility-like exceedance curves

For façade 1A only, additional comparisons were made against two situations that do not consider the presence of the soil, and which use a uniform temperature variation. This is a more common approach to modelling temperature effects; Fig. 16 demonstrates that it results in significantly more damage for this façade and might be overly conservative. Consider the crack patterns first. These correspond to the cracking situation at damage intensities around Ψ≈2. Yet the approaches with uniform temperature variations reached this state 20 °C earlier than the method proposed herein and display a larger number of cracks distributed throughout the façade. In contrast, damage for the façade, only restrained by the soil and experiencing a gradual temperature variation, is concentrated in a single crack for both positive and negative temperature gradients.

The crack patterns are consistent with the modelled situation. When the foundation is warmed up (a), it expands, which forces the façade on top of it to expand as well leading to tensile stresses in the horizontal direction and ultimately vertical cracking. Similarly, when the façade cools (e) but the foundation is unaffected by a temperature change, the façade, trying to contract, will develop horizontal tension and crack vertically. In the opposite situation, when the foundation cools (d) or the façade warms (b), the associated contraction and expansion are prevented by the façade or foundation, respectively. In these cases, the façade is forced to contract (d) or prevented from expanding (b). The masonry piers in between the openings are charged with transferring this deformation (d) or restraint (b) to the top of the façade via a shearing action. This results in rocking failure [66] of the piers with horizontal cracks at their top and bottom. The behaviour of the situation with a gradient temperature change (c and f) is more complex and was analysed in Fig. 12. However, the single crack appears towards the top of the façade instead of at the bottom region as with the other two approaches.

Finally, with Fig. 17, we take advantage of the large number of model results to determine fragility-like exceedance curves. These are elaborated by counting the number of models that, at a given temperature differential, exceed certain thresholds of damage. The curves consider both positive and temperature profiles and are segregated by façade general typology, with the reinforced (CSBR) and unreinforced (CLBR) foundations. The results are fitted to a log-normal distribution as is common practice for fragility curves [67]. This also helps to produce

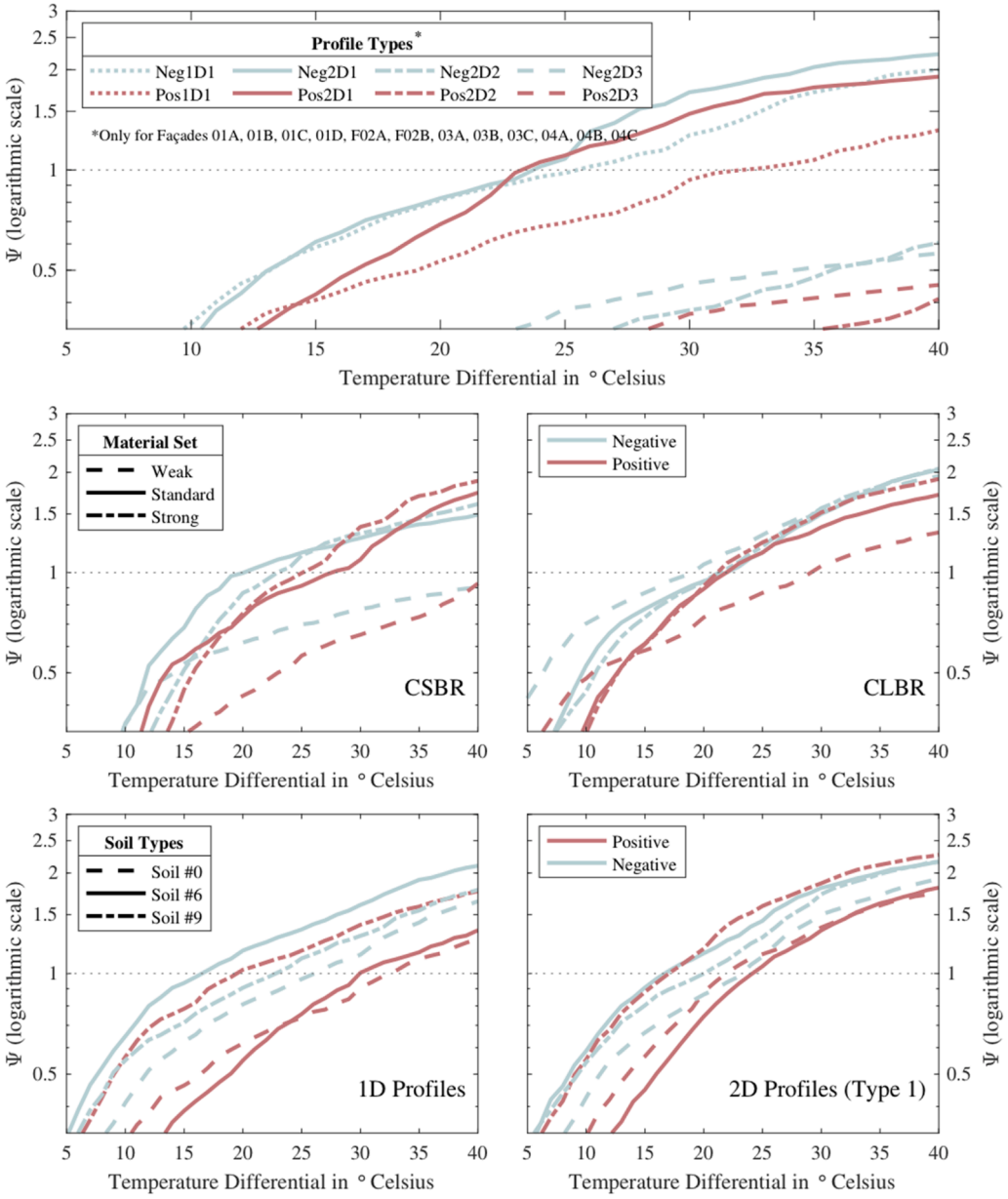

Fig. 14. Segregation by: Temperature profiles, Soil, Masonry Type, and Material Strength.

smoother curves in regions where there are few results such as at the very low bottom of the graph. Note that the lower portion of the graph is plotted with a logarithmic scale precisely to better display the very low probabilities of damage.

For temperature differentials, where one point on the façade differs in temperature to another on the opposite corner, of about 5 °C the probability of reaching or exceeding visible damage (Ψ=1) is 2 %, which can be considered very low [68]. A temperature differential of 22 °C is needed for visible damage to be expected (50 % probability) for buildings on unreinforced foundations and of 28 °C for buildings on reinforced foundations. Exceeding light damage ($\Psi \geq 3$) is not expected, in fact, for both types of masonry, the probability of exceeding light damage is below 10 % even for the 30 °C differential considered in this study. The probability of clearly visible damage with cracks of about 1 mm in width (Ψ=2) is 2 % at 10 °C for unreinforced masonry and slightly lower for reinforced foundations.

4. Discussion

The goal in this paper was to determine how sensitive masonry façades are to gradual temperature changes over their surface. While the models show that these smoother gradients, with little external restraints, will lead to damage, too, they also show that the intensity of the damage is extremely sensitive to the shape of the gradients.

4.1. Temperature and gradient shapes

The shapes assumed in this paper have been inspired by a limited number of temperature measurements on façades and other sources that depicted temperature for other purposes. A preliminary, thermography-based study [69] has confirmed that the selected shapes are possible in real world conditions though whether they are common is not discussed. Nonetheless, it is common that one corner of a façade will experience higher insolation due to shading from other buildings and the orientation of the building in respect to the sun; higher portions of the façade will experience greater insolation than those closer to the street. Walls

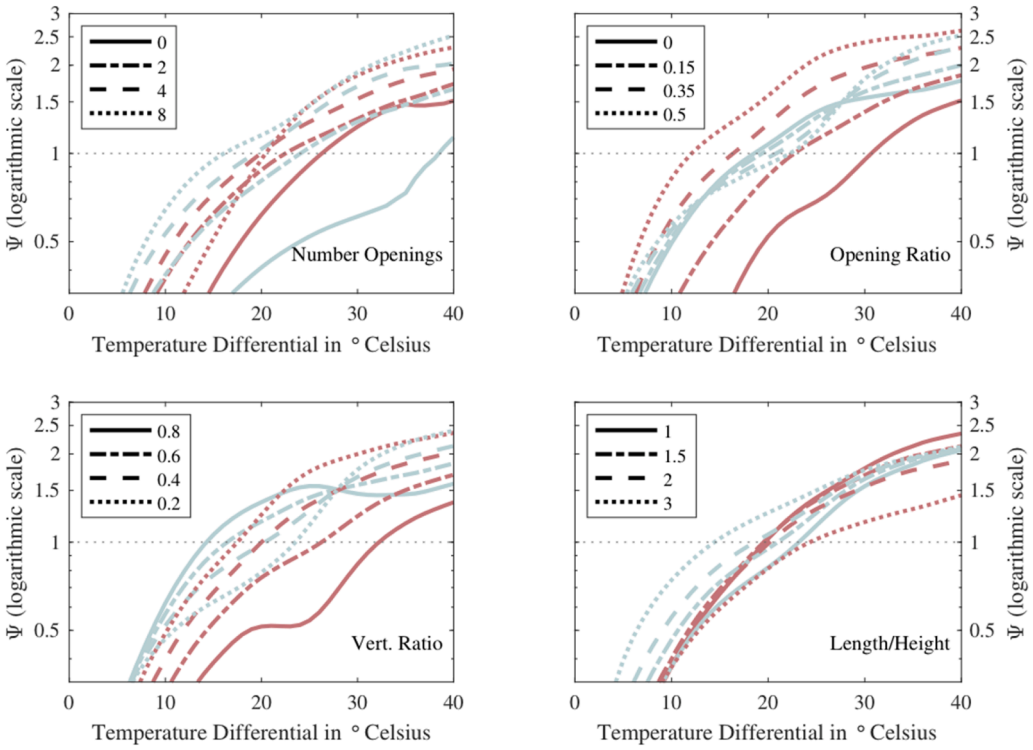

Fig. 15. Segregation by geometric properties. The curves are the means of all the façades, soils, materials, etc. but are limited to the 2D Type 1 temperature profiles.

located towards the east or west are more likely to be non-uniformly shaded due to the lower position of the sun, while southern walls (in the northern hemisphere) will face the sun higher in the sky. These relationships lead to the temperature shapes includes in this study; yet, accurate measurements, with the detail required to validate the employed shapes, are missing: brick colour, roof shape, cavity walls, and reflective surfaces will all affect the temperature shape. Hence, it is not possible to state whether the assumed shapes are conservative or optimistic, but they are possible. Certainly, in comparison to discontinuous temperature changes (Fig. 16), they appear optimistic, though smoother shapes, that affect a smaller region of the façade, will make the chosen shapes appear conservative. A parameter to determine the damage potential of temperature changes should be developed. The models presented herein will contribute to this purpose.

The temperature change over the façade dimensions is also relevant. Taller or longer façades subjected to a certain shape and differential will experience a lower damage intensity than shorter façades equally loaded, according to our models. This is because the ΔT per meter (dT/dz and/or dT/dx) is larger for the smaller façades and is congruent with the preceding paragraph. The parameter to assess temperature-effects' damaging potential should consider this. Whether shorter façades will experience similar temperature differentials has not been determined.

Regarding the magnitude of the temperature differentials, field measurements using infrared thermography on masonry façades in the Netherlands [69] recorded temperature differences of up to 13 °C between the warmest and coolest zones on a single wall surface, with values of 9–10 °C being common even when the most shaded areas were excluded. Temperature differences of 5–6 °C were also observed between perpendicular walls of the same building due to differences in solar exposure. These values are consistent with other thermographic studies: Barbero-Barrera et al. [21] measured up to 7.4 °C across a single wall in summer conditions, and Vollmer and Möllmann reported a 17 °C difference between fully sunlit and shaded portions of a house wall. The measured differentials fall well within the range where the present models predict sub-visible to visible damage (Ψ reaching 1 between 15 and 25 °C). Moreover, the distributions of measured temperature values over wall surfaces were found to be lognormal [69], indicating that extreme values are localised rather than uniformly or linearly distributed, a pattern more consistent with the gradient shapes employed herein than with uniform temperature assumptions. However, a more extensive study of temperature shapes and magnitudes on façades is needed before the fragility curves can be integrated with field data.

Besides solar radiation, temperature profiles are also influenced by a variety of factors, such as wall thickness, capacity for heat dissipation, moisture content of the air and of the façade and wall cavity (if present), heat flux toward colder areas of the façade, heating or cooling of the building interior, and the presence of other structural elements or insulation, among others. None of these factors have been considered in this study; however, our conclusions remain valid, at least for sunny days, when insolation plays the determining role in shaping façade temperature gradients.

Moreover, the transitional and cyclic nature of temperature variations has not been considered. In this study, we have included only monotonic increases or decreases in temperature. However, in real façades, temperature changes in a daily fashion. The monotonic loading employed herein thus represents the response to a single worst-case thermal event, whereas in practice damage is likely to accumulate over many smaller daily and seasonal cycles. Cyclic loading can lower effective damage thresholds through fatigue degradation of mortar joints and progressive crack opening and closing, a mechanism well documented for masonry under repeated mechanical loading [48,49]. Preliminary cyclic models, not reported in detail here, indicate that damage develops at temperature differentials approximately 10–20 % lower than the monotonic thresholds when the same gradient shape is applied repeatedly, consistent with the progressive stiffness and strength degradation observed in cyclic masonry experiments [48]. Quantifying this cyclic effect across the full parametric space requires additional models, realistic cyclic temperature profiles, and constitutive features better suited to repeated loading, such as secant unloading and reloading, and remains a key direction for future work.

Finally, we consider a uniform temperature through the thickness of the wall. In reality, the outer face a wall will be warmed when exposed to

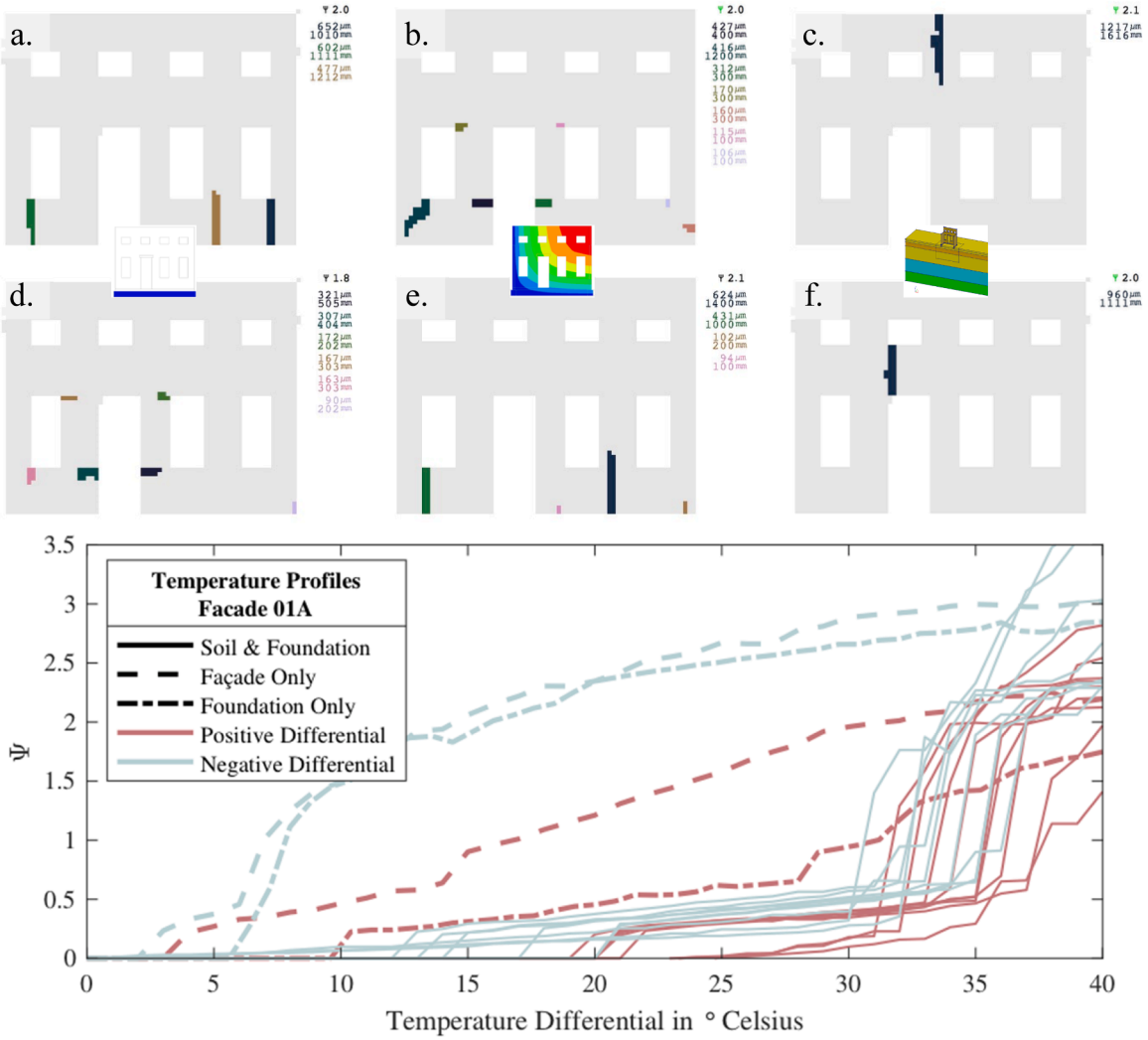

Fig. 16. Comparison for F01A with or without soil, temperature at the foundation or at the façade. See Fig. 9. Top row (a-c): temperature increase; bottom row (d-f): temperature decrease. Left column (a, d): temperature change applied to the foundation only; middle column (b, e): temperature change applied uniformly to the façade only; right column (c, f): temperature gradient applied to façade and foundation.

the sun than the inner face. For thicker walls, this effect will be more important and will require models with 3D gradient shapes which also vary in the thickness of the wall. Fully 3D models, considering also variations between adjacent walls will provide a different picture of damage; these, however, are not focus of this work.

4.2. Model aspects

Several other effects will further affect the damage estimated in this work. Foremost is that floors have not been considered as potential restraint for the temperature-induced deformations. There are multiple reasons for this. First, for the building typologies studied, timber floors provide little restraint (see also [52]). Second, floors are never directly attached to the outer leaf of a cavity wall. Typologies with stiff concrete floors, for example, are likely to employ a cavity wall system. Third, including the restraint of floors will likely result in higher damage. Neglecting the floors allows to study the effect of gradients in isolation, which is the goal of this paper. In future studies, the presence of the floors could be considered.

In a similar fashion, the properties of the soil underneath the façades have been selected; these have been estimated from the vertical shear velocity of the soil (Vs10). At first glance, the Young's moduli appear too stiff which is typical of the Vs10 approach. However, for over consolidated soil, the chosen stiffnesses can be placed on the upper bound. Moreover, for very small strains, the soil behaves stiffer, which is replicated by the selected material model [24,73]. The stiffer moduli allow greater insight into the façade damage differences generated by the studied soil profiles, since stiffer soil is likely to lead to higher damage. Given that the focus of this study is on the façades' response and not on the geotechnical one, the stiffer values are an acceptable compromise. Still, additional profiles should be included to better characterise the nuance introduced by the soil. Kruiver et al. [70,64] developed a detailed micro-zonation shear-velocity (Vs) model for the Groningen region in the Netherlands; the Vs10 and Vs15 of the three selected soil profiles (Vs10=100, 150, and 225 m/s) accurately characterise the distribution observed in the region.

Cooling temperature changes seem more damaging to the façades. However, the gradient shapes employed are more representative of solar insolation, as discussed above. Whether cooling or warming shapes are more damaging is inherently related to the location of features restraining or hindering the deformations. In this study, the soil below the foundation is mostly responsible for preventing the deformations and thus cooling shapes become more damaging. However, if building typologies include stiff restraining elements at the levels of floors or roofs, then both positive and negative temperature changes could become more, or less damaging. Nevertheless, shapes for temperature

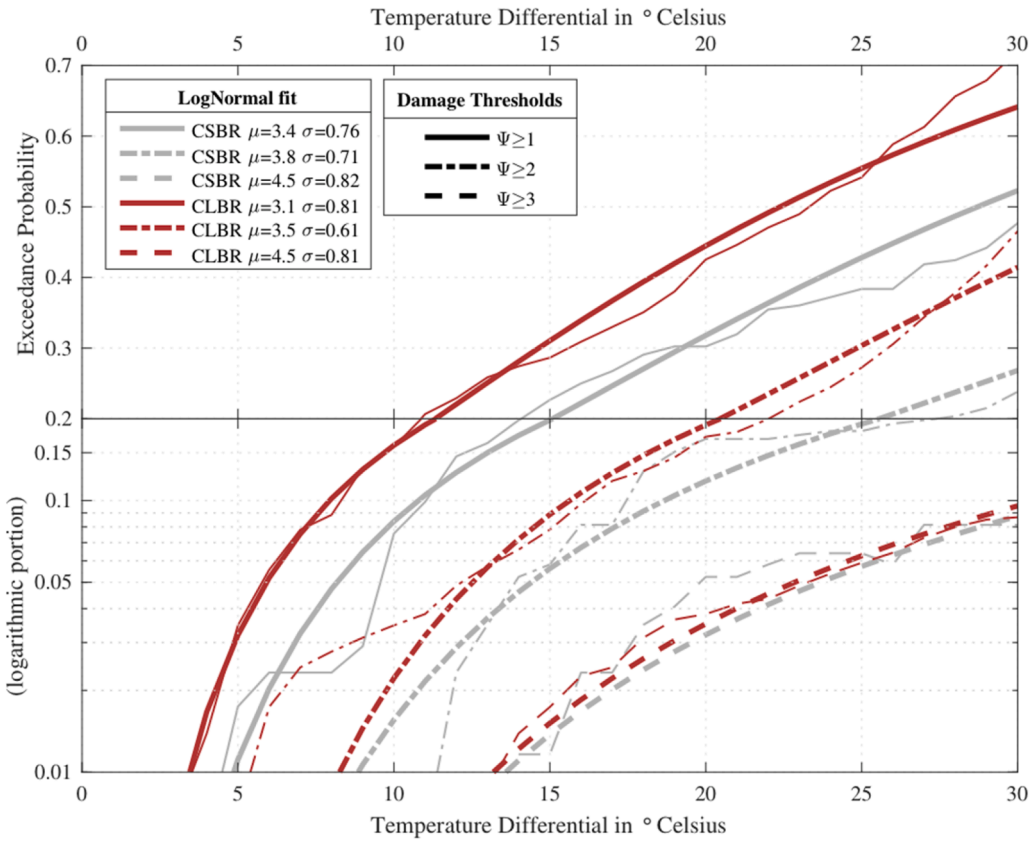

Fig. 17. Exceedance probability. CaSi vs Clay. The data between 10 °C and 25 °C is weighted twice for the lognormal fit (bold lines).

gradients more suitable for negative changes (cooling) should be explored. If these prove to be even less detrimental to the façades, then damage intensity at positive or negative temperature differentials will be more alike.

The slight differences in thermal expansion coefficient (α, CS≈8.1μ vs CL≈7.6μ; RC≈10μ) increase the differential thermal strain across the façade–foundation system for the CS-on-RC typology. For the same ΔT, $\Delta\varepsilon=\Delta\alpha\cdot\Delta T$ at the masonry–concrete interface is larger, which increases the horizontal tensile stresses in the piers near the foundation and magnifies crack localisation. This is consistent with the modest left shift of the CSBR curves relative to CLBR in Fig. 14 at Ψ≈1. This effect is amplified in façades with more modern layouts (larger/more openings, lower vertical-masonry ratio; Fig. 15), where reduced shear transfer area raises stress concentrations for a given temperature strain. Together, the α-mismatch and reduced vertical continuity explain the slightly larger damage propensity observed for CaSi façades on RC strips and for the "modern" geometries, even when soil profile and gradient shape are held constant.

A small point regarding the chosen element types in the numerical models must be discussed. In our models, we employ solid elements for the masonry façade. Shell elements would also be possible and are likely to lead to different results. For comparison, shell-based façades could be explored. This would also allow the use of other material models more suited to masonry such as the Engineering Masonry Model [27], though modifications would be required as this model does not include thermo-mechanical coupling [28]. This could be particularly relevant when modelling cyclic temperature changes, either due to daily or seasonal temperature variations, as the EMM includes features more suited for this purpose than the TSRCM, such as secant unloading and reloading for shear.

4.3. Cracking patterns

The models show cracking developing around openings and at the edges of the façades. This is compatible with cracking observed in real buildings [55,59]. However, whether cracking in buildings is uniquely due to temperature effects is difficult to determine. Fig. 18 shows the recurrence of cracking for each façade. This is not the cracking intensity (that is consistent for every façade with Ψ≤2) but highlights instead the location where cracks are most common in the analyses of this study. For many façades cracks underneath windows on the ground floor or at the top corner of openings are very common. Most cracks are vertical. Cracks also propagate from the openings to the edges of the façade. Again, this agrees with existing knowledge [63]. The models reveal, however, that some façades (like F01A, F03A or F04B) display cracking localised in specific areas regardless of temperature shape, soil profile, etc., while others (like F01G, F03D, or F09B) present a damage picture that changes depending on each parameter varied. For the latter cases, employing reference literature to diagnose whether cracks are temperature-related will be less effective.

Cracking will also be affected by other damaging hazards. If settlement-induced cracks are present, they will modify the temperature-induced cracking pattern. Similarly, temperature-induced cracking will modify the structural response to other hazards such as settlements or vibrations.

Conventional numerical approaches to thermal loading in masonry typically assume a uniform temperature change applied to an idealised, fully restrained wall. While computationally convenient, such simplifications tend to overestimate damage potential. Dilrukshi & Dias [11] showed that under uniform temperature changes, walls subjected to high restraint stiffness quickly exceed tensile capacity; however, when partial restraints or flexible foundations are introduced, crack initiation is delayed and crack widths are reduced. Bejarano-Urrego et al. [25], using discrete crack modelling, found that the predicted number and

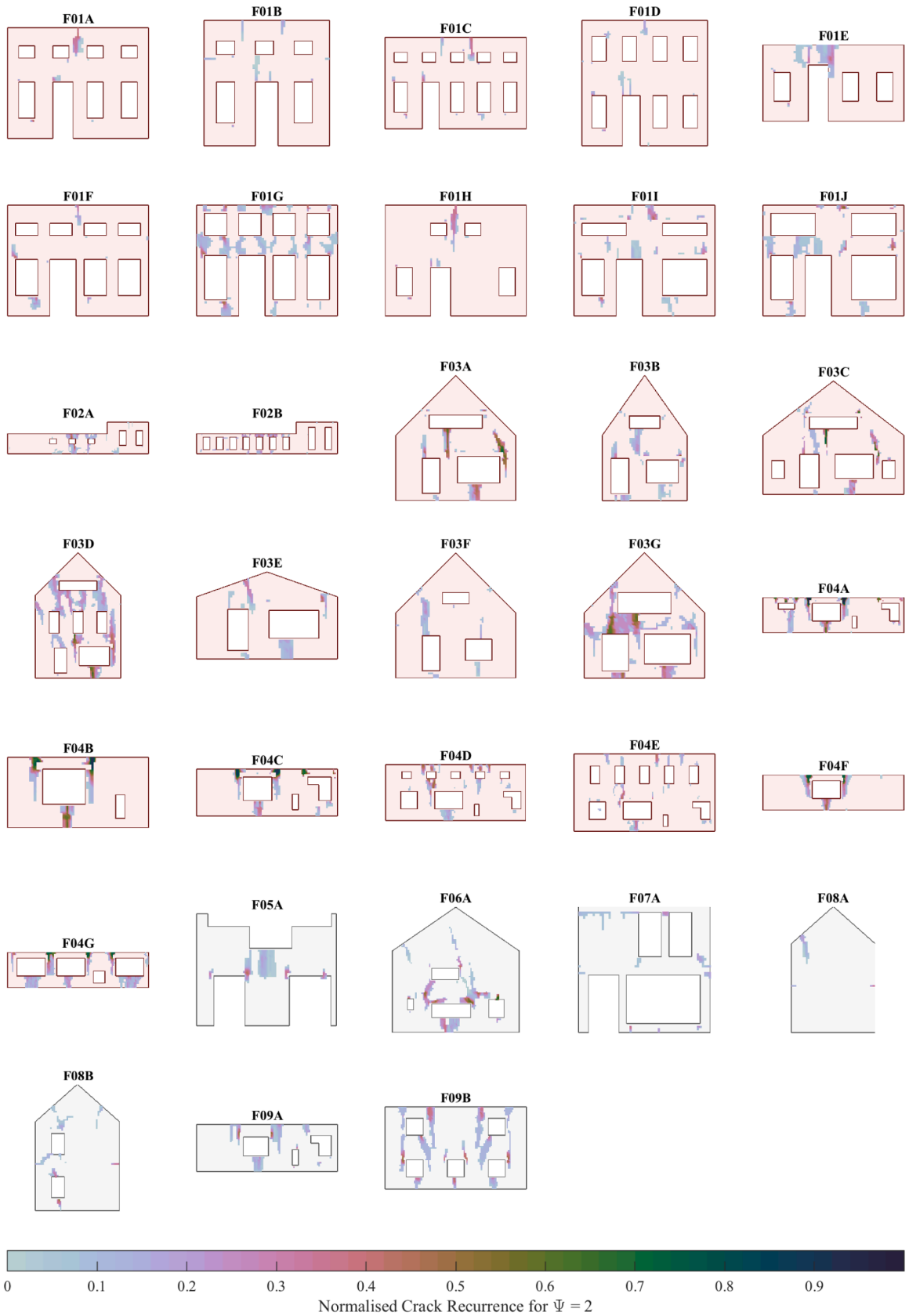

Fig. 18. "Heat-map" of crack recurrence. Darker areas indicate regions where models display cracks more frequently, with fully dark areas indicating that all models showed cracking at the marked location.

orientation of cracks changes markedly when non-uniform boundary stiffness and load profiles are considered, with uniform temperature steps often producing unrealistic, evenly spaced cracking across the wall.

While many studies, damage reports, and real-estate agencies characterise cracks in masonry as a consequence of temperature effects, none provide a link between (spatially) measured temperatures and cracking monitoring. The models herein have proven that spatial variations can lead to damage, yet, this remains an important validation study for the models; see later "Validation".

4.4. Comparisons against other modelling studies

Prakash et al. [26] extended this by integrating shrinkage, creep, and stiffness evolution into a micro-modelling framework, demonstrating that the interaction between early-age shrinkage and thermal loads can either accelerate or inhibit cracking depending on restraint location and compliance. Their work also emphasised that models ignoring these effects misrepresent crack initiation thresholds, sometimes by more than 10 °C. Lagier et al. [15] and Briffaut et al. [29] further quantified how the shape and timing of temperature changes influence stress development: gradual or localised gradients produced lower peak stresses and fewer cracks than sudden, uniform changes, even under the same total temperature differential.

Advanced constitutive modelling, as implemented by van Zijl et al. [16], enables tensile softening, fracture energy dissipation, and anisotropic response to be captured within a coupled thermal–mechanical framework. Such models, while not incorporating soil–structure interaction, still demonstrate how the form of the applied thermal field governs the localisation of tensile zones and the mode of cracking. Barbero-Barrera et al. [21] and Ferreira et al. [22], though not modelling cracking, underscore through empirical measurement that actual façade temperature fields are often far from uniform, with sharp localised peaks driven by shading, orientation, and architectural features, conditions under which simple uniform-load models become least representative.

The approach adopted here advances beyond these simpler treatments by combining three elements rarely addressed together: (1) explicit representation of façade–foundation–soil interaction, allowing restraint stiffness to emerge naturally from the coupled system; (2) application of empirically inspired, non-uniform temperature profiles that reflect realistic gradients rather than idealised steps; and (3) a constitutive law capable of simulating progressive tensile damage and crack localisation. This combination mitigates the over-conservatism inherent in uniform-load, over-restrained methods, yielding more realistic deformation compatibility and better alignment with observed damage patterns. As a result, the predicted probability of visible damage at given temperature differentials is more representative of actual structural performance, providing a stronger foundation for diagnostic assessments and retrofit prioritisation in masonry structures.

4.5. Validation

Direct, building-specific validation of thermal cracking thresholds would require co-located monitoring of façade temperature fields, crack evolution, and restraint conditions, which is not available for (historical) masonry. The validation provided here is therefore indirect and at several levels and is meant to anchor the modelling choices already discussed.

In particular, the thermal loading is supported by the thermography evidence and discussion already presented (Fig. 2 and [69]): the order of magnitude and non-uniform character of the applied gradients are observed in practice, which underpins the chosen gradient families. Likewise, damage is interpreted through the crack-based index Ψ, and its practical link to measurable crack networks in masonry has been demonstrated in the experimental/DIC example (Fig. 4) and linked to finite-element-method modelling strategies.

Finally, the benchmark comparisons against conventional idealisations (Fig. 16) serve as a credibility check: the coupled façade–foundation–soil models with gradual gradients reproduce the expected shift relative to uniform, fully restrained analyses (later initiation and more localised cracking), while the simulated crack locations and recurrence patterns (Figs. 12 and 18) align with the common façade crack morphologies referenced earlier and observed in practice. Together, these elements provide a coherent (if necessarily partial) validation that the proposed framework captures the governing mechanisms, even though comprehensive field datasets to validate ΔT–Ψ thresholds remain a key gap for future work.

5. Conclusions

This study examined whether realistic, non-uniform temperature gradients, acting on largely unrestrained façades but with restraint from the underlying soil, can generate the cracking patterns often observed in practice. Using homogenised continuum modelling with tensile softening and explicit façade–foundation–soil interaction, 1200 variants were explored across geometry, materials, soils, and gradient shapes. Three key findings are identified: First, gradient shape and location are decisive: wide, vertically distributed gradients (Shape 1) produce visible damage ($\Psi \geq 1$) at temperature differentials roughly half those needed for concentrated gradients (Shapes 2, 3). Second, restraint stiffness governs severity: stiff sandy soils suppress free thermal movement, increasing tensile stresses; softer soils allow accommodation and delay cracking. Third, geometry determines damage: more openings and lower vertical masonry ratios promote earlier localisation, whereas the length/height ratio is of secondary importance for temperature actions.

A unifying observation is that the slope of the temperature field where restraint is effective controls damage. Larger $\partial T/\partial z$ (or $\partial T/\partial x$) near the restraint—in this study, the foundation and its soil—drives higher damage intensity. For example, with Shape 1 on stiff soil, visible damage became likely at $\Delta T \approx 20$ °C for warming and ≈ 25 °C for cooling, whereas Shapes 2–3 often required > 35 °C. Fragility-like exceedance curves showed that visible cracking ($\Psi \geq 1$) can occur from ΔT as low as 5 °C, especially for cooling profiles, but widespread visible damage was unlikely below $\Delta T \approx 15$–20 °C in the studied cases.

Compared to common simplified approaches—uniform temperature steps on fully restrained walls—this method predicts later crack initiation, fewer cracks, and patterns consistent with expected deformation compatibility. The uniform-temperature models reached $\Psi \approx 2$ (clearly visible cracks) some 15–20 °C earlier and produced unrealistic distributed cracking, highlighting the over-conservatism of such methods.

Beyond these findings, the results highlight gaps in current knowledge. High-resolution, façade-scale temperature datasets are scarce, limiting validation of gradient shapes. Cyclic and seasonal effects, moisture–temperature coupling, and the role of additional restraints (floors, roof diaphragms, cavity ties) remain largely unquantified. Material properties should be measured under relevant thermal–mechanical loading rates, and 3D effects such as out-of-plane bowing and pier–spandrel interaction need further study. From a practical standpoint:

- Measure or estimate actual gradient shapes instead of assuming uniform fields.
- Prioritise façades where the location of large $\partial T/\partial z$ coincides with stiff restraints.
- Expect single dominant cracks at heights where gradient slope intersects stiffness changes.
- Reduce gradient (e.g. shading, insulation) or restraint (e.g. joints, foundation compliance) at these critical heights to lower damage risk.

In short, temperature-induced façade damage is driven more by

gradient–restraint interaction than by peak temperature alone. Larger $\partial T/\partial z$ closer to restraints will lead to higher damage intensity, and both models and measurements should be organised around this principle.

Declaration of generative AI and AI-assisted technologies in the manuscript preparation process

During the preparation of this work the author(s) used OpenAI's ChatGPT to check for grammar, spelling and other inconsistencies in the text.

After using this tool/service, the author(s) reviewed and edited the content as needed and take(s) full responsibility for the content of the published article.

CRediT authorship contribution statement

Paul A. Korswagen: Writing – review & editing, Writing – original draft, Supervision, Project administration, Methodology, Formal analysis, Conceptualization. **Michele Longo:** Writing – review & editing, Investigation, Formal analysis. **Alfonso Prosperi:** Writing – review & editing.

Declaration of competing interest

The authors declare the following financial interests/personal relationships which may be considered as potential competing interests:

The authors report financial support was provided by Instituut Mijnbouwschade Groningen. If there are other authors, they declare that they have no known competing financial interests or personal relationships that could have appeared to influence the work reported in this paper.

Acknowledgments

The authors would like to acknowledge the contribution of IMG and CM for inspiring this study. In addition, discussions and comments by em.prof. Jan Rots greatly helped to shape our work.

Supplementary materials

Supplementary material associated with this article can be found, in the online version, at doi:10.1016/j.rineng.2026.109810.

Data availability

Data can be found at the 4TU repository under doi:10.4121/454833f7-0fa3-4080-ae8e-6e5a8752b1d9. Additional data will be made available on request.

References

[1] M. Girardi, C. Padovani, D. Pellegrini, Influence of temperature on the structural behaviour of masonry buildings, 12th Int. Conf. Struct. Anal. Hist. Constr. (2020). SAHC 2020.

[2] F. Ferretti, M. Canestri, C. Mazzotti, Effect of temperature variations on the bond behavior of FRCM applied to masonry, Mater. Struct. 55 (2022) 166, https://doi.org/10.1617/s11527-022-02002-x, 2022.

[3] C. Guenser, P. Morenon, N. Domede, S. Corn, M. Salgues, Thermo-mechanical analysis of a stone masonry wall subjected to fire using FEM and DEM approaches, IB2MaC 2024 Proc. (2025), https://doi.org/10.1007/978-3-031-73310-9_39.

[4] O.R. El-Zaroug, J.P. Forth, J.Q. Ye, A.W. Beeby, Prediction of thermal cracking In concrete structures reinforced with GFRP, FRPRCS11 Proc. (2013).

[5] B. Klemczak, A. Smolana, Multi-step procedure for predicting early-age thermal cracking risk in mass concrete structures, Mater. (Basel) 2024 (2024) 3700, https://doi.org/10.3390/ma17153700, 17.

[6] B. Sujatha, B.A. Kumar, Effect of expansion joints on dynamic analysis of structures, Int. J. Sci. Eng. Adv. Technol. IJSEAT 4 (2) (2016).

[7] Ł. Kapusta, L. Szojda, The role of expansion joints for traditional buildings affected by the curvature of the mining area, Eng Fail Anal 128 (2021) (2021) 105598, https://doi.org/10.1016/j.engfailanal.2021.105598.

[8] K.G.S. Dilrukshi, W.P.S. Dias, R.K.N.D. Rajapakse, Numerical modelling of cracks in masonry walls due to thermal movements in an overlying slab, Eng. Struct. 32 (2010) (2010) 1411–1422, https://doi.org/10.1016/j.engstruct.2010.01.019.

[9] M. Mosoarca, A.I. Keller, C. Petrus, A. Racolta, Failure analysis of historical buildings due to climate change, Eng Fail Anal 82 (2017) (2017) 666–680, https://doi.org/10.1016/j.engfailanal.2017.06.013.

[10] J.L. Lerma, C. Mileto, F. Vegas, M. Cabrelles, Visible and thermal IR documentation of a masonry brickwork building, XXI Int. CIPA Symp. (2007).

[11] K.G.S. Dilrukshi, W.P.S. Dias, Field survey and numerical modelling of cracking in masonry walls due to thermal movements of an overlying slab, J Natl Sci Found 36 (3) (2008) 205–213, 2008.

[12] E. Bauer, P.M. Milhomem, L.A. Gimenez Aidar, Evaluating the damage degree of cracking In facades using infrared thermography, J. Civ. Struct. Health Monit. 8 (2018) 517–528, https://doi.org/10.1007/s13349-018-0289-0.

[13] M.M. Resende, E.B. Gambare, L.A. Silva, Y.d. Cordeiro, E. Almeida, R.P. Salvador, Infrared thermal imaging to inspect pathologies on façades of historical buildings: a case study on the municipal market of Sao Paulo, Braz., Case Stud. Constr. Mater. 16 (2022) (2022) e01122, https://doi.org/10.1016/j.cscm.2022.e01122.

[14] D. Mrozek, M. Mrozek, J. Fedorowicz, Analysis of an effectiveness of expansion joints in the multi-family building loaded by mining activities, J. Civ. Eng. Environ. Archit. JCEEA 64 (2/II/17) (2017) 197–208, https://doi.org/10.7862/rb.2017.92, tXXXIVzkwiecień-czerwiec 2017s.

[15] F. Lagier, X. Jourdain, C. De Sa, F. Benboudjema, J.B. Colliat, Numerical strategies for prediction of drying cracks in heterogeneous materials: comparison upon experimental results, Eng. Struct. 33 (2011) (2011) 920–931, https://doi.org/10.1016/j.engstruct.2010.12.013.

[16] G.P.A.G. van Zijl, P.A. de Vries, A.T. Vermeltfoort, Masonry wall damage by restraint to shrinkage, J. Struct, Eng 130 (7) (2019) 1075–1086, https://doi.org/10.1061/(ASCE)0733-9445(2004)130:7(1075), 2004.

[17] A. Yüksel, M. Arıcı, H. Karabay, Comparison of thermal response times of historical and modern building wall materials, J. Therm. Eng. 7 (6) (2021) 1506–1518, https://doi.org/10.18186/thermal.991093.

[18] D. Pellegrini, A. Barontini, M. Girardi, P.B. Lourenço, M.G. Masciotta, N. Mendes, C. Padovani, L.F. Ramos, Effects of temperature variations on the modal properties of masonry structures: an experimental-based numerical modelling approach, Structures 53 (2023) (2023) 595–613, https://doi.org/10.1016/j.istruc.2023.04.080.

[19] G. Ferrarini, Evaluation of Thermal Heat Fluxes In Buildings with Infrared Thermography, Universita degli Studi di Padova, 2016.

[20] R. Ramirez, B. Ghiassi, P. Pineda, P.B. Lourenço, Hygro-Thermo-mechanical analysis of brick masonry walls subjected to environmental actions, Appl. Sci. 2023 (13) (2023) 4514, https://doi.org/10.3390/app13074514.

[21] M.d. Barbero-Barrera, R. Tendero-Caballero, M.G. de Viedma-Santoro, Impact of solar shading on façades' Surface temperatures under summer and winter conditions by IR thermography, Architecture 2024 (4) (2024) 221–246, https://doi.org/10.3390/architecture4020014.

[22] C. Ferreira, C. Sousa, R. Faria, M. Azenha, M. Pimentel, Thermo-hygro-mechanical simulation of cracking in thick restrained RC members: application to a 50 cm thick slab, J. Adv. Concr. Technol. 17 (2019) 489–505, https://doi.org/10.3151/jact.17.7.489.

[23] A.J.P. Castello, M.F.H. de Carvalho, L.T.M. Mota, C.C. Pezzuto, Comportamento Térmico De Fachadas Urbanas Com Diferentes Revestimentos Cerâmicos, XVII Encontro Nacional de Conforto no Ambiente Construído, 2023.

[24] P.C. Van Staalduinen, K. Terwel, J.G. Rots, Onderzoek Naar de Oorzaken van Bouwkundige Schade in Groningen Methodologie En Case Studies Ter Duiding Van De Oorzaken, Delft University of Technology, 2018. Report number CM-2018-0111 July 2018 - Downloadable from, www.NationaalCoordinatorGroningen.nl.

[25] L. Bejarano-Urrego, E. Verstrynge, G. Giardina, K. Van Balen, Crack growth in masonry: numerical analysis and sensitivity study for discrete and smeared Crack modelling, Eng. Struct. 165 (2018) (2018) 471–485, https://doi.org/10.1016/j.engstruct.2018.03.030.

[26] P.R. Prakash, M. Azenha, J.M. Pereira, P.B. Lourenço, Finite element based micro modelling of masonry walls subjected to fire exposure: framework validation and structural implications, Eng. Struct. 213 (2020) (2020) 110545, https://doi.org/10.1016/j.engstruct.2020.110545.

[27] G.M.A. Schreppers, A. Garofano, F. Messali, J.G. Rots, DIANA validation report for masonry modelling, DIANA FEA rep. 2016-DIANA-R1601 TU Delft Struct. Mech. Rep. CM-2016-17 (2016) 143.

[28] M. Sousamli, Orthotropic Cyclic Continuum Constitutive Model For Masonry Structures and Comparative Studies, TU Delft, 2024.

[29] M. Briffaut, F. Benboudjema, J.M. Torrenti, G. Nahas, Numerical analysis of the thermal active restrained shrinkage ring test to study the early age behavior of massive concrete structures, Eng. Struct. 33 (2011) (2011) 1390–1401, https://doi.org/10.1016/j.engstruct.2010.12.044.

[30] G.P.A.G. van Zijl, R. de Borst, J.G. Rots, Finite element analysis of cracking due to shrinkage. Fracture Mechanics of Concrete Structures Proceedings FRAMCOS-3, 1998.

[31] D. González-Aguilera, S. Lagüela, P. Rodríguez-Gonzálvez, D. Hernández-López, Image-based thermographic modeling for, Assess. Energy Effic. Build. Facades, Energy Build. 65 (2013) (2013) 29–36, https://doi.org/10.1016/j.enbuild.2013.05.040.

[32] A.D. Tzenkov, M.V. Schwager, Nonlinear FEM analysis of the seismic behavior of the menta bituminous-face rockfill dam. Numerical analysis of dams, Lect. Notes Civ. Eng. 91 (2021), https://doi.org/10.1007/978-3-030-51085-5_35.

[33] J.L. Lerma, M. Cabrelles, C. Portalés, Multitemporal thermal analysis to detect moisture on a building façade, Constr. Build. Mater. 25 (2011) (2011) 2190–2197, https://doi.org/10.1016/j.conbuildmat.2010.10.007.
[34] B. Tejedor, M. Casals, M. Gangolells, X. Roca, Quantitative internal infrared thermography for determining In-situ thermal behaviour of facades, Energy Build 151 (2017) (2017) 187–197, https://doi.org/10.1016/j.enbuild.2017.06.040.
[35] A. Azarnejad, A. Mahdavi, The solid thermal conductivity of building masonry bricks and The temperature dependence of The thermal conductivity of bricks, Energy Procedia 78 (2015) 1720–1725, https://doi.org/10.1016/j.egypro.2015.11.277.
[36] S. Bagavathiappan, B.B. Lahiri, T. Saravanan, J. Philip, T. Jayakumar, Infrared thermography for condition monitoring – A review, Infrared Phys Technol 60 (2013) (2013) 35–55, https://doi.org/10.1016/j.infrared.2013.03.006.
[37] F. Benboudjema, F. Meftah, J.M. Torrenti, Interaction between drying, shrinkage, creep and cracking phenomena in concrete, Eng. Struct. 27 (2005) (2005) 239–250, https://doi.org/10.1016/j.engstruct.2004.09.012.
[38] P. Bison, A. Bortolin, G. Cadelano, G. Ferrarini, F. Peron, X. Maldague (2014). Inspecting the facade of an historical building by transient solar heating and IR thermography. Conference Paper.
[39] M.D. Boscardin, E.J. Cording, Building response to excavation-induced settlement, J. Geotech. Eng. 115 (1) (1989) 1–21, 1989.
[40] S.A. Sazonova, S.D. Nikolenko, N.V. Akamsina, Consideration of temperature stresses In the calculation of crack formation, Concr. Massifs Build., IOP Conf, Ser,: Mater. Sci. Eng. 1079 (2021) (2021) 032027, https://doi.org/10.1088/1757-899X/1079/3/032027.
[41] J.B. Burland, B.B. Broms, V.F.B.D. Mello, Behaviour of foundations and structures, Build. Res. Establ. (1977).
[42] M.B. Gaggero, P.A. Korswagen, R. Esposito, J.G. Rots, Innovative application of self-healing technology to masonry: a proof of concept, Int. J. Archit. Herit. (2024), https://doi.org/10.1080/15583058.2024.2380408.
[43] H. Cifuentes, F. Montero-Chacón, J. Galán, J. Cabezas, A. Martínez-De la Concha, A finite element-based methodology for the thermo-mechanical analysis of early age behavior in concrete structures, Int. J. Concr. Struct. Mater. 13 (2019) 41, https://doi.org/10.1186/s40069-019-0353-0.
[44] O. Deck, H. Anirudh, Numerical study of the soil–structure interaction within mining subsidence areas, Comput. Geotech. 37 (2010) (2010) 802–816, https://doi.org/10.1016/j.compgeo.2010.07.001.
[45] H. Glavaš, M. Hadzima-Nyarko, I.H. Buljan, T. Baric, Locating hidden elements in walls of cultural heritage buildings by using infrared thermography, Build. 2019 9 (2019) 32, https://doi.org/10.3390/buildings9020032.
[46] B. González-Rodrigo, R. Tendero-Caballero, M. García-De-Viedma, J. Pestana-Puerta, A. Carrio-Fernández, J. Sánchez-López, R. Suárez-Fernández, P. Campoy-Cervera, J. Bonatti-González, J.G. Rejas-Ayuga, R. Martínez-Marín, M. Marchamalo-Sacristán, Monitorización Del Comportamiento Térmico De Fachadas Mediante UAV: aplicaciones en La Rehabilitación De Edificios, Dyna Cod, 7899 | Tecnol. constr. | 3305,34 Topogr. edif. (2016), https://doi.org/10.6036/7899.
[47] S. Govindjee, G.J. Kay, J.C. Simo, Anisotropic modelling and numerical simulation of brittle damage in concrete, Int. J. Numer. Methods Eng. 38 (1995) (1995) 3611–3633.
[48] P.A. Korswagen, M. Longo, E. Meulman, J.G. Rots, Crack initiation and propagation in unreinforced masonry specimens subjected to repeated in-plane loading during light damage, Bull. Earthq. Eng. (2019), https://doi.org/10.1007/s10518-018-00553-5.
[49] P.A. Korswagen, M. Longo, J.G. Rots, Fragility curves for light damage of clay masonry walls subjected to seismic vibrations, Bull. Earthq. Eng. 2022 (20) (2022) 6193–6227, https://doi.org/10.1007/s10518-022-01404-0.
[50] P.A. Korswagen, M. Longo, A. Prosperi, J.G. Rots, K.C. Terwel, Modelling of damage in historical masonry façades subjected to a combination of ground settlement and vibrations. SAHC 2023, RILEM Bookseries 47 (2023) 904–917, https://doi.org/10.1007/978-3-031-39603-8_73, 2024.
[51] R. Latifi, M. Hadzima-Nyarko, D. Radu, R. Rouhi, A brief overview on crack patterns, repair and strengthening of historical masonry structures, Mater. (Basel) 16 (2023) 1882, https://doi.org/10.3390/ma16051882, 2023.
[52] A. Prosperi, M. Longo, P.A. Korswagen, M. Korff, J.G. Rots, 2D and 3D modelling strategies to reproduce the response of historical masonry buildings subjected to settlements, Int. J. Archit. Herit. (2024), https://doi.org/10.1080/15583058.2024.2325472.
[53] J.G. Rots, Smeared and discrete representations of localized fracture, Int. J. Fract. 51 (1990) 45–59, https://doi.org/10.1007/BF00020852.
[54] J.G. Rots, R. Van Der Pluijm, A.T. Vermeltfoort (1997). Structural masonry - an experimental/numerical basis for practical design rules. Balkema - ISBN 90 5410 680 8.
[55] A. Tavukcuoglu, S. Akevren, E. Grinzato, In situ examination of structural cracks at historic masonry structures by quantitative infrared thermography and ultrasonic testing, J. Mod. Opt. 57 (18) (2010) 1779–1789, https://doi.org/10.1080/09500340.2010.484553, 20 October.
[56] J. Gomes de Freitas, H. Carasek, O. Cascudo, Utilização de Termografia Infravermelha Para Avaliação De Fissuras em Fachadas com Revestimento De Argamassa E Pintura, Ambiente Construído Porto Alegre 14 (1) (2014) 57–73, vn.
[57] S. Jafari, R. Esposito, J.G. Rots, F. Messali, Characterizing the material properties of Dutch unreinforced masonry, Procedia Eng 193 (2017) 250–257.
[58] S. Sfarra, E. Marcucci, D. Ambrosini, D. Paoletti, Infrared exploration of the architectural heritage: from passive Infrared thermography to hybrid Infrared thermography (HIRT) approach, Mater. Constr. Vol 66 (323) (2016), https://doi.org/10.3989/mc.2016.07415.
[59] A. Prosperi, P.A. Korswagen, M. Korff, R. Schipper, J.G. Rots, Empirical fragility and ROC curves for masonry buildings subjected to settlements, J. Build. Eng. 68 (2023) (2023) 106094, https://doi.org/10.1016/j.jobe.2023.106094.
[60] SBR, Schade aan Gebouwen, SBR, 2010.
[61] M. Mulder, P. Perey, B. Scholtens, G. de Kam, G. Perlaviciute, Gas production and earthquakes in Groningen - reflection on economic and social consequences, Cent. Energy Econ. Res. - CEER - Policy Pap. (2018). | no. 3 | June 2018.
[62] A. Prosperi, M. Longo, P.A. Korswagen, G. Giardina, J.G. Rots, Comparative study of NLFE models for simulating settlement-induced damage in masonry façades: macro- and simplified micro-models, Front, Built Env. 11 (2025) 1618329, https://doi.org/10.3389/fbuil.2025.1618329.
[63] P. Korswagen, M. Longo, E. Meulman, J.G. Rots, Experimental and computational study of the influence of pre-damage patterns in unreinforced masonry crack propagation due to induced, repeated earthquakes, in: 13th North American Masonry Conference, 2019.
[64] P. Kruiver, G. de Lange, A. Wiersma, P. Meijers, M. Korff, J. Peeters, J. Stafleu, R. Harting, R. Dambrink, F. Busschers, J. Gunnink, Geological Schematisation of the Shallow Subsurface of Groningen - for Site Response to Earthquakes for the Groningen Gas Field, 5, Deltares, 2015, 1209862-005-GEO-0004Version16 March 2015final.
[65] P. Korswagen, M. Longo, J. Rots, GEMMA: Research into the Combined Effects of Soil Strains, Soil Curvatures and Earthquake Vibrations from Multiple Mining Activities on Damage in Masonry, Delft University of Technology, 2024. Report Number 01, FinalSeptember 13, 2024.
[66] F. Messali, J.G. Rots, In-plane drift capacity at near collapse of rocking unreinforced calcium silicate and clay masonry piers, Eng. Struct. 164 (2018) (2018) 183–194.
[67] P. Gehl, D.M. Seyedi, J. Douglas, Vector-valued fragility functions for seismic risk evaluation, Bull Earthq. Eng 11 (2013) (2013) 365–384, https://doi.org/10.1007/s10518-012-9402-7.
[68] B.v. Tiel, U. Sauerland, M. Franke, Meaning and use in the expression of estimative probability, Open Mind: Discov. Cogn. Sci. 6 (2022) 250–263, https://doi.org/10.1162/opmi_a_00066.
[69] A. Prosperi, P.A Korswagen, M. Longo, J.G Rots, Infrared thermography for spatial variations of surface temperature on masonry walls: deepening the understanding of their damaging potential, Front, Built Env., - Constr. Mater. (2026). Accepted.
[70] P.P. Kruiver, E. van Dedem, R. Romijn, G. de Lange, M. Korff, J. Stafleu, J. L. Gunnink, A. Rodriguez-Marek, J.J. Bommer, J. van Elk, D. Doornhof, An integrated shear-wave velocity model for the Groningen gas field, Bull Earthq Eng 15 (2017) 3555–3580, https://doi.org/10.1007/s10518-017-0105-y.
[71] https://manuals.dianafea.com/d107/en/1181807-1192485-total-strain-crack-models.html Retrieved May 2025.
[72] https://manuals.dianafea.com/d107/en/1181807-1182193-extended-hardening-soil-model.html Retrieved May 2025.